POLITECNICO DI TORINO

Collegio di Ingegneria Chimica e dei Materiali

Corso di Laurea Magistrale
in Ingegneria Chimica e dei Processi Sostenibili

Tesi di Laurea Magistrale

CFD MODELLING OF THE PNEUMATIC CONVEYING OF NON-CONVENTIONAL SOLIDS

Relatori

prof. Daniele Marchisio
firma del relatore (dei relatori)

Candidato

Simone Termini
firma del candidato

Novembre 2022

Contents

Notations

r_T	0.95	
C_D	drag coefficient	
d	particle diameter	[mm]
D	pipe diameter	[mm]
e_{ss}	coefficient of restitution	
f	friction factor	
F_{fw}	fluid wall attrition coefficient	
F_{pw}	particle wall attrition coefficient	
g	gravitational acceleration	[m^2/s]
$g_{0,ss}$	radial distribution function	
G_s	solid mass flowrate	[kg/s]
L	pipe length	[m]
N_p	number of parcels	
p_s	solid pressure	[Pa]
P	pressure	[Pa]
R	bend radius	[m]
r_N	normal momentum retained	
r_T	tangential momentum retained	
Re	particle Reynolds	
$\mathbf{u_f}$	fluid velocity	[m/s]
$\mathbf{u_p}$	particle velocity	[m/s]
$\mathbf{v_{r,s}}$	particle terminal velocity	[m/s]

ε	Turbulent energy dispersion rate	$[m^2/s^3]$
θ_{cp}	close-pack particle volume fraction	
θ_f	fluid volume fraction	
θ_p	particle volume fraction	
Θ_s	granular temperature	$[m^2/s^2]$
λ_s	granular viscosity	[Pa s]
μ_f	fluid viscosity	[Pa s]
μ_s	solid shear viscosity	[Pa s]
ρ_f	fluid density	$[kg/m^3]$
ρ_p	particle density	$[kg/m^3]$
τ_f	fluid stress tensor	[Pa]
τ_s	solid stress tensor	[Pa]
ψ	Particle sphericity	
ν_f	Fluid kinematic viscosity	$[m^2/s^2]$

1. Introduction

Pneumatic conveying is a unit operation in which a solid, fed from a hooper or a bin, is entrained by a gas at high velocity. This technology can be conducted in different configurations, such as horizontal or vertical pipelines, and different operative conditions, to what concerns the solid concentration, the gas velocity, and the operative pressure.

Pneumatic conveying is currently used in many industrial fields as it enables to convey a broad range of different granular solids, and it is dependable even to transport high value products and is a self-cleaning operation. On the other side it requires to be meticulously designed, to avoid wear equipment problems and product degradation; this can be a challenging task as different flow pattern can verify.

To help the design of this operation CFD tool is often used to develop a model that can describe this operation. The frameworks that can suit the modeling of the pneumatic conveying are the continuum ones, or Eulerian-Eulerian, that can be used in dilute systems and the discrete ones or Eulerian-Lagrangian, that are more expensive in terms of computational time but are dependable also with dense phase systems [1]. After choosing a framework, one way to develop a model involves the comparison of the simulations with experimental data, Tebianian et al. [2]. Within this procedure the measured variable is selected as reference, and the model parameters are varied to study how they impact the simulation and subsequently tune them. The following work has been conducted during an Internship at the Solaize's site of the company IFP Energies Nouvelles, has the task of testing three different approaches to model the pneumatic conveying operation. For this purpose, an article from literature is selected, to make comparisons between the simulated and experimental data, and, for each framework, a tuning on the parameters is done to find the ones that fit the best.

The following chapters will describe the subjected in greater detailed; in chapter 2 the key features of the pneumatic conveying operation are described, in chapter 3 the main results of the selected article from literature are resumed. Moreover, the geometry used to execute the simulations is depicted and it is explained how the variable of interest are obtain from the simulation. In chapter 4 the theoretical bases of the tested frameworks are presented, while in chapters 5,6 and 7 for each framework evaluated the simulation set-up and results are discussed. Finally, chapter 8 is dedicated to final considerations and proposal for further investigations.

2. Pneumatic Conveying

Pneumatic transport, or pneumatic conveying, consists of the transport of granular solids in a gas stream, which normally is air, but, in presence of combustible dust, N_2 is employed. This kind of technology applies to a very wide variety of particles, with some limitations in the maximum average diameter, which must be smaller than 30 [mm], and the content of humidity, which must be under 30 %. For this reason, pneumatic conveying systems are employed in a very wide range of applications in the chemical, pharmaceutical, and food industry.

This operation can be conducted in many different pathways, such as horizontal and vertical pipes; it is also possible to impose changing of direction in the pipeline, with bends or Tee junctions. Moreover, an important advantage, is that this kind of transport is self-cleaning, and, in general, it is suitable to high-value products. As it is easy to automatize and control this kind of operation the workforce required is low.

Nevertheless, pneumatic conveying requires high specific power, and so, typically, the majority of the application of this technology involves fine powders; abrasive and friable materials, especially when the system is operating at high gas velocities should be avoided.

A critical issue of this technology is related to the wear of the equipment, it is possible to convey material up to hundreds of meters. Another crucial point, as it will be further described, involves the complexity of the flow type that makes it difficult to design and maintain the system.

The pneumatic conveying line can be subdivided o four different zones; the prime mover provides the operative fluid flowrate, and pressure, necessary to perform the transportation of the granular solids; it is constituted by compressors, and fans, when the operation is conducted with positive pressure, and vacuum pumps when the system undergoes to negative pressure. The following section is the feeding, mixing, and acceleration zone where the solid, initially at rest is introduced typically in a horizontal pipe using a feeder and encounters the fluid flux resulting in acceleration and consequently important change in its momentum. The subsequent section is the conveying zone, which is constituted by the conveying pipe which can follow vastly different pathways; one key role plays the proper selection of the material, which must satisfy the characteristic of the conveyed product, for example in terms of abrasiveness. The last section is the gas-solid separation zone, where the conveyed material must be separated from the gas phase in which it has been transported.

2.1 Pneumatic Conveying Systems

The pneumatic conveying circuit system, based on the pressure at which the circuit operates, can be classified in positive pressure, negative pressure, or a combination of both.

2.1.1 Positive Pressure Configuration

In fig.2.1 is shown an example of a positive pressure system. This kind of systems are typically employed to move the solid from the storage hopper to receiving bins, where the amount of material received by the bins is controlled by several diverter valves. To keep the system under pressure and maintain the gas at the designed volumetric flowrate a blower,

which is a volumetric compressor, is used. Typically, the operating Pressure is 1 [barg] and, as the storage hopper operates at atmospheric pressure, a device is necessary to feed the solid.

One possibility is to employ a rotary valve, which is a rotary item that allows for keeping the solid flowrate at the desired value.

When one deals with big superficial gas velocities it is also possible to operate with a venturi injector, to feed the solid it is also possible to use a venturi injector, where a restriction in the section of the conveying pipe is created in correspondence with the hooper to transport the solid in the main conveying pipe.

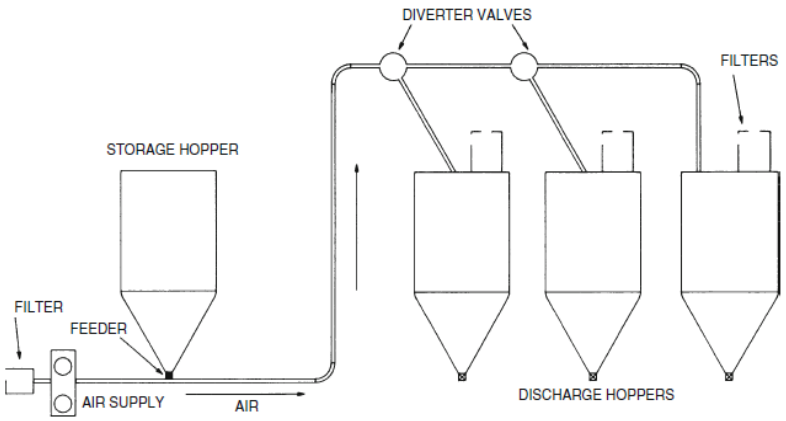

Figure 2.1: positive pressure system from Klinzing et al. [5] modified

2.1.2 Negative Pressure Configuration

In Fig.2.2 is shown an example of a negative pressure system. This kind of system is used to collect the granular material present at different points of the factory to a common point, or for raw material arriving in the factory. The desired degree of vacuum is obtained through a liquid ring pump, typically these systems operate at 0,4-0,5 [bar], to avoid damage at the vacuum pump, after delivering the solid at the discharge hooper, the air is filtered in a filter bag. This kind of system allows the management of toxic and polluting material, as a pipe leakage will not release material into the environment, as the system operates in vacuum conditions.

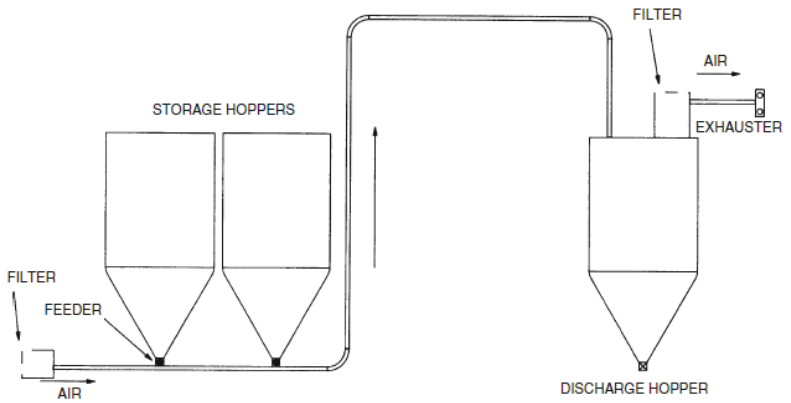

Figure 2.2: negative pressure system from Klinzing et al.[5] modified

2.1.3 Combined Negative-Positive Pressure Configuration

In Fig.2.3 is shown an example of a negative-positive pressure system. In this configuration, the circuit that operates at positive pressure receives feeding the discharge of the one operating at vacuum condition. These systems are very versatile and, in terms of pipe, broader than the previous ones. The part operating in vacuum conditions is served by the liquid ring pump, while the other part is kept under pressure by a volumetric compressor.

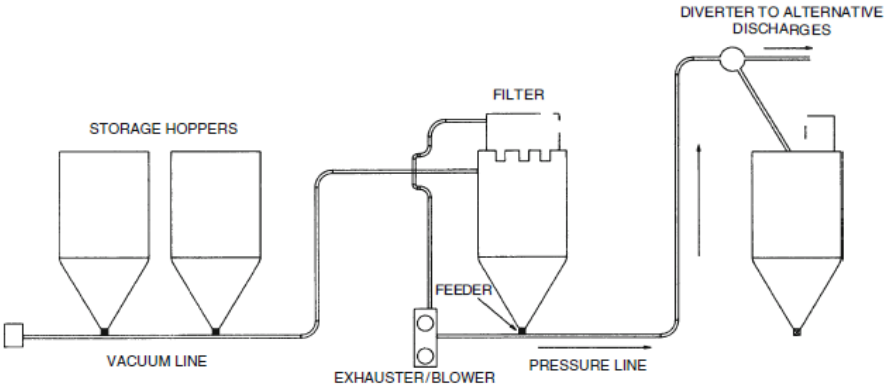

Figure 2.3: combined negative-positive pressure system from Klinzing et al. [5] modified

2.2 Pneumatic Conveying Regimes

Pneumatic conveying can be performed in two different regimes: dilute and dense phase. The dilute phase is characterized by high gas velocities, in general, greater than 20 [m/s] low solids concentrations, less than 1% in volume, and low pressure drops per unit length, less than 5 [mbar/m]. This kind of application, because of the high energy expenditure required to compress the gaseous phase, in the face of the small amount of product transported, is feasible only for short pathways. Moreover, to avoid abrasion of the solid and damage to the pipeline, the solid flowrate must be under 10 [t/h].

Dense phase pneumatic conveying systems are instead characterized by smaller superficial gas velocities, typically between 1 and 5 [m/s], solids concentrations bigger than 30 % and pressure drops per unit length in the order of magnitude of 20 [mbar/m]. This makes the dense phase flow attractive, as it is possible to transport a larger quantity of solid per unit of gas, lowering in this way the energy consumption. Moreover, as the superficial gas velocity is lower than the one in dilute phase transport, pipe erosion and damage to the product are significantly reduced.

The particles' behavior in these two regimes is quite different: in the case of the dilute phase the particles are fully suspended, and each particle behaves as an individual, for this reason, the fluid-particle interactions overcome the particle-particle interactions, which are negligible. The opposite verifies in the case of the dense phase regime: as the particle concentration increase, the particle-particle interactions become increasingly relevant and prevail over the particle-fluid ones, moreover, the particles are not anymore fully suspended.

It must be remarked that only in the case of dilute phase transport it is possible to operate under vacuum. It must be considered that in literature a recognized threshold to clearly distinguish the border between these two regimes, in fact, according to Konrad et al.[3] there are many possible parameters through which is possible to make a distinction, such as the

ratio between the solid and gas mass flowrates, solid concentration and cross-section fraction free for the passage of the fluid.

According to Rhodes et al. [4] and Klinzing et al. [5], to establish the boundary between the two regimes, at a fixed solid flowrate, it is considered a minimum superficial gas velocity required to perform dilute phase pneumatic conveying. This limit is named saltation velocity in horizontal flow, and chocking velocity in vertical flow. To determine these values, it must be obtained the state diagram also known as Zenz diagram, which represents the pressure drops per unit length of the pipeline at fixed solid flowrate as a function of the superficial air velocity. It must be pointed out that, in contrast to dilute phase, it does not exist only one flow type in the dense phase regime, but many, in both horizontal and vertical pneumatic conveying, are possible, as showed in Fig.2.4.

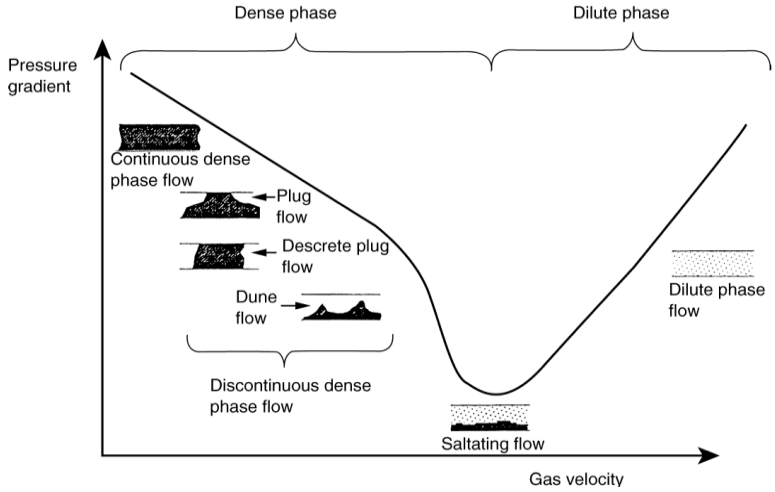

Figure 2.4: phase diagram for horizontal pneumatic transport from Rhodes et al.[4] modified

2.2.1 Dense Phase Regime

As shown in figure 2.4 the dense phase transport could be subdivided in two main regimes: continuous and discontinuous dense phase flow.

In the continuous dense phase flow the solid fill the entire pipe section and it is necessary to provide high gas pressure. This kind of transport is suitable for granular material with a narrow particle size distribution and application that does not involve a long route.

The discontinuous dense phase flow is classifiable in three different regimes: dune flow, discrete plug flow and plug flow. In the dune flow regime, the solid tends to stratify in correspondence with the wall pipe and move toward the pipeline as dunes.

In the discrete plug flow regime solid plugs occupy the entire cross-section of the pipe, instead, the plug flow regime, is a fusion between the previous two, as the solid moves in form of dunes occupying the entire pipe cross-section. On the boundary between the dense and the dilute phase regime, another flow pattern is present, known as saltating flow; this regime is unstable, as a slight variation in the superficial can produce great variations on the flow, and is characterized by a layer of settled particles upon which some particles are entrained.

The distance that occurs before an entrained particle in this regime will settle is named saltation length. Operating in the dense phase regime can be advantageous as the concentration of mass of the product per unit of gas phase flowrate is larger, this translates

into a smaller energy cost per unit of product recovery and easier gas-solid separation at the end of the conveying line. However, the gas pressure requires to perform the operation is remarkably high, and, especially in the discontinuous dense phase, it is difficult to model properly the system, and blockage of the section can occur.

2.3 Vertical pneumatic conveying

In figure 2.5 is depicted the dilute part of a state, or Zenz, diagram, as the Pressure Gradient, defined as $\Delta P/\Delta L$, is plotted at constant solid mass flowrate, as a function or the superficial gas velocity, at higher solid flowrate each curve is shifted on the right. In this diagram the line AB represents the characteristic curve when only air is present on the system. Considering the curve corresponding to $G=G_1$ it is possible to distinguish two regions, as $\Delta P/\Delta L$ reach a minimum with the increase of the superficial air velocity before rising again.

At low superficial gas velocities, the static head of the solids prevails, while, as the velocity is increased, the friction resistance force starts dominating over the static head of solids. At high superficial gas velocity, the concentration of the solid particles, and so, the particle volume fraction inside the pipeline increases while the particle velocity tends to decrease. As the solid static heads is directly proportional to the particle volume fraction, this term will grow in this region, whereas the friction resistance term is proportional, respectively, in the case of the solid to the square of the particle velocity, and in that of gas to the square of the superficial gas velocity. When the curve reaches point E, the gas is no longer able to transport all the solid, and the condition of chocking is reached, as the system approaches the dense phase region.

The system in general, as described in Grace et al. [9] can experience diverse types of chocking, classified as A,B and C. Type A verifies when the solid particles progressively are no longer suspended and the solid tends to accumulate in correspondence of the wall generating a dense phase. This condition occurs in correspondence of the accumulative chocking velocity, and it is the minimum superficial gas velocity that guarantees that the particles are fully suspended without accumulation in the lower part of the pipeline. Type B is characterized by a strong instability in the system, so from an industrial point of view it is the most undesirable condition; it can be the result of the interaction between the gas blower and the conveyor or between the solid feeder and the conveyor. Type C, or classical chocking, occurs at smaller superficial gas velocity in comparison with type A, and it is not representable with a unique value, as it takes place in an extended range of velocities, and is characterized by instability.

A crucial point is that type A and type B chocking can happen in all type of systems, but type C do not. In fact, if the diameter of the particle is small, or the vertical pipe diameter is large, the particles cannot reach the wall of the pipeline; this kind of system are said no slugging system.

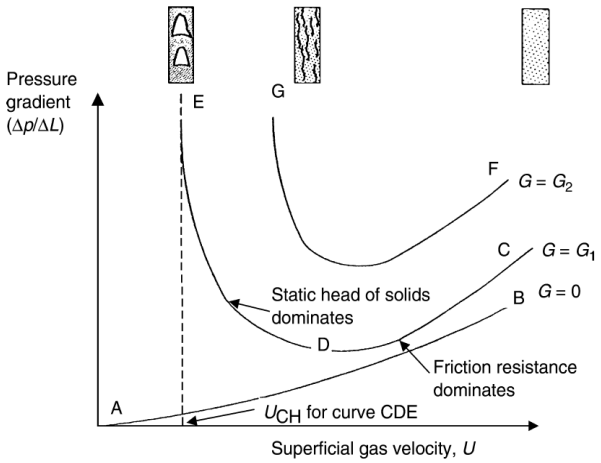

Figure 2.5: phase diagram for vertical pneumatic transport from Rhodes et al.[4] modified

2.4 Horizontal pneumatic conveying

In Fig. 2.6 the dilute phase part of the state diagram for a horizontal pneumatic transport line is shown. The AB curve corresponds to air only situation, while the other curves, from downwards to upwards, show the characteristic of the circuit when the solid mass flowrate is increased. In this case, being the pipeline horizontal, the static head contribution to the pressure drops is null, so, in the pressure drops equation (2.1) the only term that is influenced by the superficial air velocity is the frictional one.

Considering the curve at $G=G_1$, if the superficial gas velocity is decrease below point D, the solid is not kept suspended anymore and start to settle down in the bottom of the pipeline, further decreasing will make the system to reach the dense phase condition; the superficial gas velocity corresponding to point D is named saltation velocity.

This velocity is a cut off value that identifies whether a solid particle will be indefinitely transport for an infinite length or will stop to a distance named saltation length. Even if the operative superficial gas velocity is smaller than the saltation velocity, the particle will not settle down if the length of the route is smaller than the saltation length, as result from Rabinovich et al. [10].

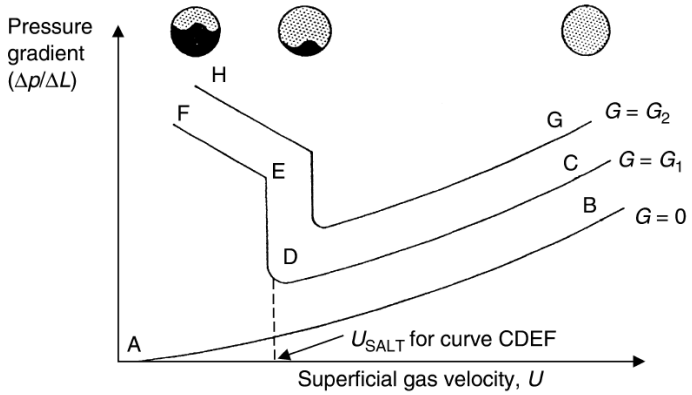

Figure 2.6: phase diagram for horizontal pneumatic transport from Rhodes et al. [4] modified

2.5 Bend Region

Studying the flux of a fluid phase towards a bend, it has been seen, from Boothroyd et al. [11] that double vortex regime occurs; this phenomenon even worse in the presence of a biphasic gas-solid flow. In fact, when the solids enter the bend, experience a strong centrifugal force, resulting in a zig-zag pathways. Because of that the particles slow down as they cross the bend, to be re-accelerated as thy pass the bend, because of this the solid particle volume fraction downstream the bend is significantly higher. This is more evident for a bend connecting a vertical trait followed by a horizontal one: in this case the particles can settle down along a significant trait before being entrained again. For this reason, it is a good practice try to minimize the number of bends in a conveying line.

2.6 Pressure drops

The pressure drops on a pneumatic conveying line are due to different contributions: particle acceleration, gas-wall and solid-wall friction, gas, and solids static head. To obtain a general expression for the pressure drops a momentum balance considering an infinitesimal length of a pipe, resulting in:

$$\Delta p = \frac{1}{2}\theta_f \mathbf{u}_f^2 + \frac{1}{2}\theta_p \mathbf{u}_p^2 + F_{fw}L + F_{pw}L + \rho_f L\theta_f \mathbf{g}\sin\varphi + \rho_p L\theta_p \mathbf{g}\sin\varphi \tag{2.1}$$

Where θ_p is the particle volume fraction, θ_f is the fluid volume fraction and φ is the angle formed between the pipe and the horizontal axis. It can be noted that, as in the horizontal configuration φ is zero, the solid and the gas static heads terms are null. The main difficult is insight the evaluation of the friction terms, which simplified when the system operates in the dilute regime, as it is assumed that the gas-wall friction term is independent from the presence of the solid. In this case, it is possible to identify a pressure drops term only caused by the solid and one to the presence of the gas and evaluate them separately as described in Mason et al.[7] and Hirokata et al. [8]:

$$\Delta p = \Delta p_s + \Delta p_g + \Delta p_h \tag{2.3}$$

Where (2.2) is applied in horizontal transport, and (2.3) in case of vertical transport. In both equations appear the terms Δp_s and Δp_g, that are evaluated with the same approach, since the phenomena influencing the pressure drops in the system are the same. The gas contribution is modeled as the sum of acceleration and friction term:

$$\Delta p = \frac{1}{2}\theta_f \mathbf{u}_f^2 + F_{fw}L \tag{2.4}$$

Where the friction term is expressed with Fanning equation:

$$F_{fw} = \frac{2f\rho_g \mathbf{u}_f^2}{D_t} \tag{2.5}$$

Where the friction factor f is expressed with the Colebrook-White equation:

$$\frac{1}{\sqrt{f}} = -2\log\left[\frac{\theta_f}{2.7D_t} + \frac{2.51}{\mathrm{Re}\sqrt{f}}\right] \tag{2.6}$$

Similarly, to the gas phase, the solid phase contribution is evaluated as:

$$\Delta p_s = \frac{1}{2}\theta_p \rho_p \mathbf{u}_p^2 + F_{pw}L \tag{2.7}$$

Where the first term is the contribution of the acceleration of the solid, and the second term is the wall-solid friction contribution. The solid-wall friction coefficient is evaluated thanks to the correlation developed in Hirokata et al.[8]:

$$F_{pw} = \frac{0.057\, G_s}{\sqrt{D_t\, \mathbf{g}}} \tag{2.8}$$

The static head term is expressed as:

$$\Delta p_h = \theta_p \rho_p L\mathbf{g} + \theta_f \rho_f L\mathbf{g} \tag{2.9}$$

Where the first term represents the contribution of the solid and the second the contribution of the gas. One should note that, as the density of a gas is three orders of magnitude smaller than that of a solid, the second term, especially when the system operates in dense regime, is normally negligible.

3. Bibliographical research

The Bibliographical research was conducted to find in literature an experimental work regarding pneumatic conveying, in which at least two independent macroscopical variables were obtained. The selected article from Fei et al.[6] has the purpose to investigate a pneumatic conveying line, depicted below in Fig.3.1, operating in dilute phase regime. First goal of the authors was to find the operative condition, in terms of R/D and superficial gas velocity, for which the pressure drops of the line reached a minimum, to minimize the energy expense at the compressor. The second goal was to find for which conditions the particle velocity at the first bend was minimized, as this guarantee to minimize the pipe erosion problems, which is an important drawback of the pneumatic conveying, especially when operating in dilute phase regime, condition characterized by high superficial gas velocities.

3.1 Experimental Set-up

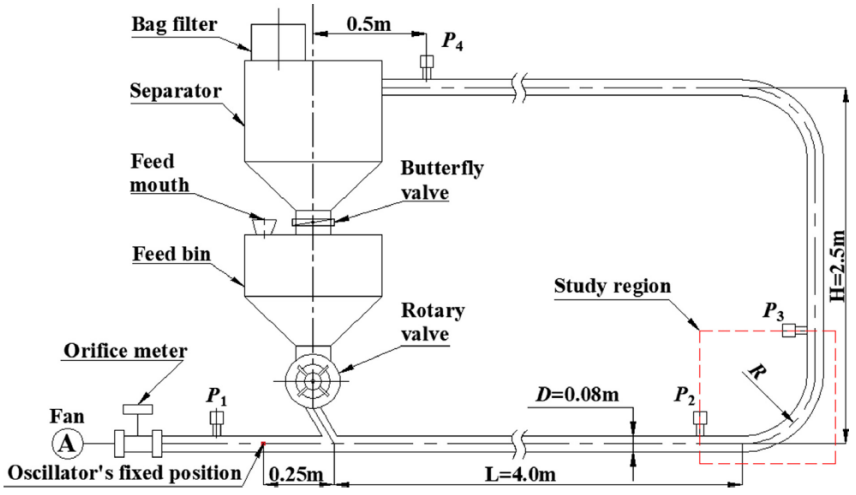

Figure 3.1: Process outline from Fei et al. [6] modified

The conveying line depicted in fig. 3.1, was employed to perform pneumatic conveying experiments, in dilute phase regime using air as gas phase and polyethylene particles and solid phase. Aim of the work was to study the line pressure drops, measured along with pressure transducers, defined as:

$$\Delta p_{line} = \Delta p_1 - \Delta p_4 \tag{3.1}$$

Moreover, the axial and radial component of the particle velocity in correspondence of the first bend are obtained thanks to the Particle image velocimetry (PIV) technique. The experiments were performed at P and T ambient with a constant particle flowrate of 0.29 [kg/s], and equal radius bend in the upper and lower part of the line. During the experiments three different radius bend are evaluated:

- R= 0.5 [m], with a ratio between the bend radius and the line diameter of 6.25
- R= 0.4 [m], with a ratio between the bend radius and the line diameter of 5
- R= 0.3 [m], with a ratio between the bend radius and the line diameter of 3.75

For each configuration, the variables of interest described above, for each R/D ratio are obtained, varying the superficial air velocity in the range of 14-21 [m/s].

3.2 Particles

In figure 3.2 the particle size distribution of the polyethylene particles employed to perform the experiments is showed; in the paper other particle characteristics are indicated, as the particle density, and the particle bulk density, respectively equals to 945 and 597 [kg/m^3].

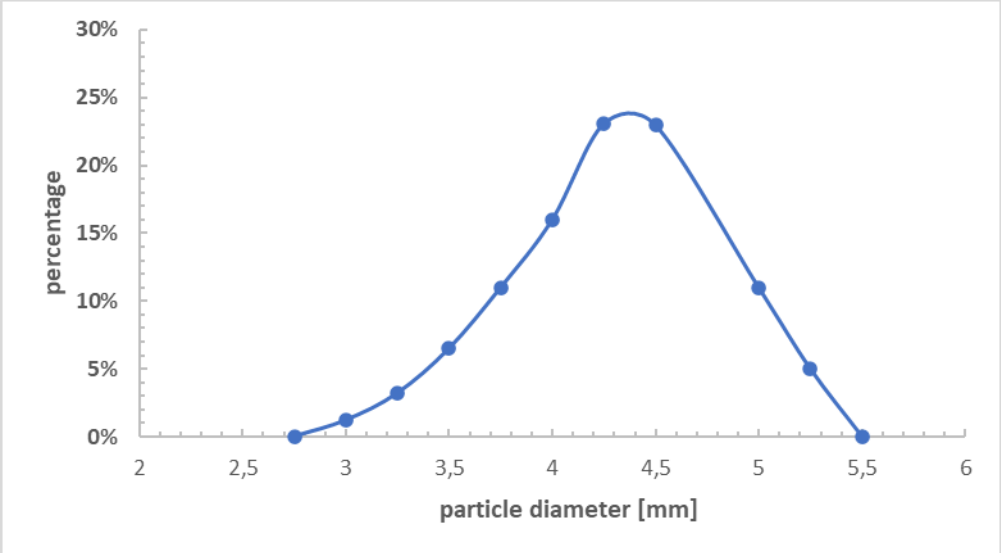

Figure 3.2: Particle size distribution

According to the Geldart classification, showed in Fig.3.3, that classifies the particles based on their densities and diameters, these particles correspond to class D; characterized by big dimensions and large densities, they are known as spoutable, definition that considers their fluidization properties. Starting from a condition where these particles are in a fixed bed condition and feeding a gas stream at the bottom of the bed, the gas will tend to rise the bed in the form of large bubbles that will tend quickly to coalesce each other, leading to spouting as they reach the top of the bed. The fluidization of this kind of particle is exploited in equipment know as spouted bed that find their application in fields such as coating, drying, surface modification, and polyethylene production.

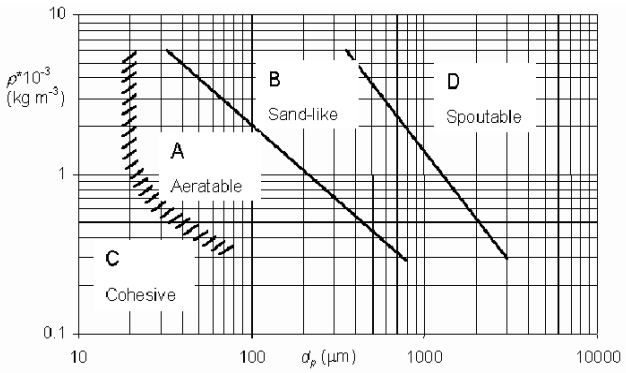

Figure 3.3: Geldart classification

From Fig. 3.4 and 3.5 one should note that the particles are ellipsoidal and mostly the particle's sphericity lies in 0.75-0.8 range.

Figure 3.4: particles shape from Fei et al. [1] modified

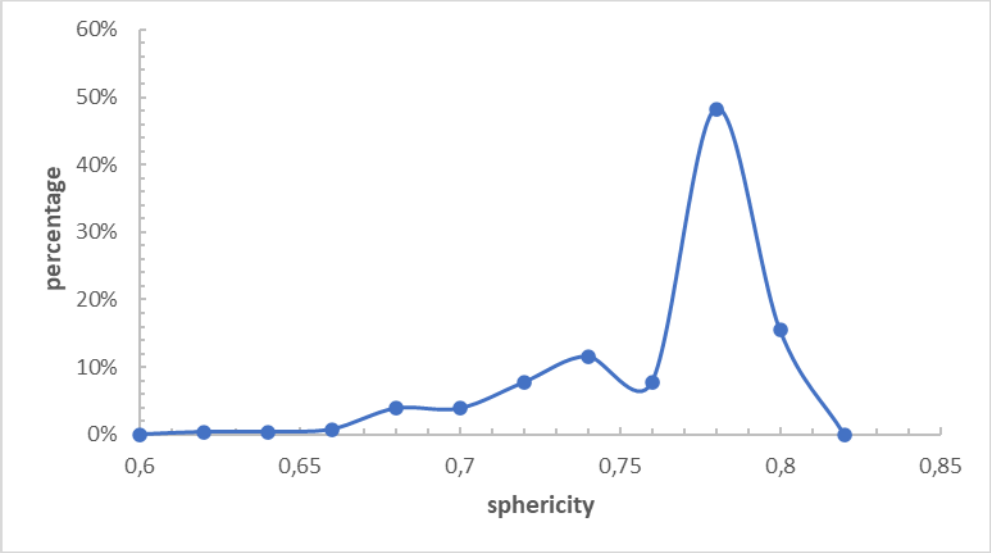

Figure 3.5: Particle sphericity distribution

3.3 Pneumatic conveying line Pressure Drops

In Fig. 3.6 the line pressure drops, for each R/D ratio, as function of the superficial air velocity, are depicted. As the superficial air velocity is increased, the pressure drops first tends to reduce, reaching a minimum, and then starts to rise again, after reach a minimum in correspondence of the minimum pressure drop velocity. As R/D is decreased, at equal superficial air velocity, the pressure drops tend to increase. This is related to the fact that, when colliding against the pipe wall, the particles tend to lose their momentum, slowing down. The energy needed to re-accelerate the particle is given by the air, and this translate to bigger pressure drops. If the curvature bend curvature radius is increased, the pathway that the particle must cover will increase, and so the number of collisions will decrease, resulting in smaller values of line pressure drops.

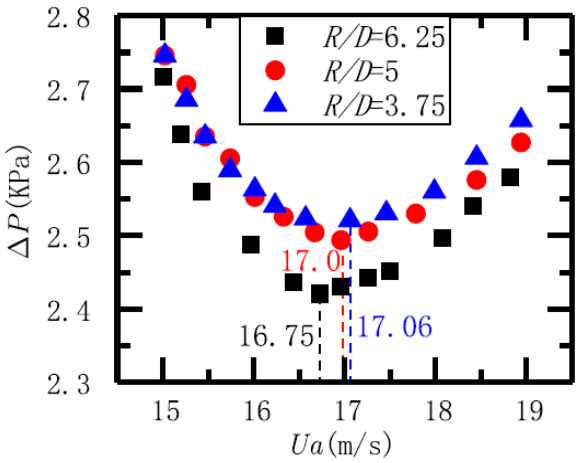

Figure 3.6: Pipeline Pressure drops from Fei et al.[6] modified

3.4 PIV analysis

The particle imagine velocimetry (PIV) technique is a non-intrusive measurement technique in which employs a laser to illuminate a flow plane, represented in this case by the x-z plane according to the reference system in Fig. 3.9, and a camera to capture particles images. The particle images are then processed by an acquisition system to convert them into velocity fields. In Fig 3.7 the experimental set-up to acquire the radial and the axial averaged particle velocities is shown. The experiments are conducted at a superficial air velocity equal to the minimum pressure drop velocity for each R/D configurations by employing a high-speed camera and measuring the particle velocities distribution with respect to the plane passing through the center of the pipe. The angle φ results from the direction of z-axis and that of gravity, and u_p and ω_p are respectively the axial and the radial particle velocity component at the bend. In the article the results are reported averaging both velocities in time and normalizing the results with respect to the minimum pressure drops velocity.

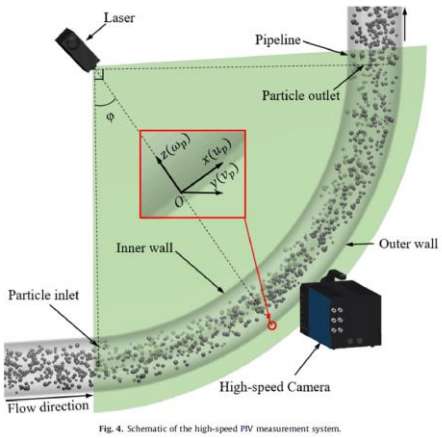

Figure 3.7: PIV analysis from Fei et al.[6] modified

In Fig. 3.8 (a) the normalized averaged axial particle velocity as function of angle φ is shown. The trend of the curve is similar for all the configurations considered, in the region between $0 \leq \varphi \leq 20°$ it remains constant, as there are not many collisions between the particles and the

pipe wall, and this leads to little energy loss of the particles, which will not slow down a lot. In the following region, between 20° ≤ φ ≤ 40°, the normalized averaged axial particle velocity drops more steeply as R/D is decreased: since number of collisions between the particles and the pipe wall increases as the bend curvature radius augments resulting in more accentuating particles' slowing down. In the final region the three configurations exhibit different behavior, with R/D = 6 the normalized averaged axial particle velocity continues to decrease with the same slope of the previous region, while in the cases R/D = 3.75 and R/D =5 the normalized averaged axial particle velocity remains constant after being decreasing very steeply in the previous region. It should be stressed that at the bend outlet the normalized averaged axial particle velocity reaches the same value. The trend of normalized averaged radial particle velocity along with φ is depicted in Fig. 3.8 (b): initially, due to particles' inertia, for all the configurations, between 0° ≤ φ ≤ 43°, it assumes negative values, which corresponds to outer wall pipe direction. In the following region, in the cases with R/D=5, and R/D = 3.75, it reaches a maximum before going to zero proceeding towards the outlet of the bend, while, for R/D=6.25 it remains constant. It should be underline that as R/D is increased the radial component of particles' motion becomes smaller and smaller.

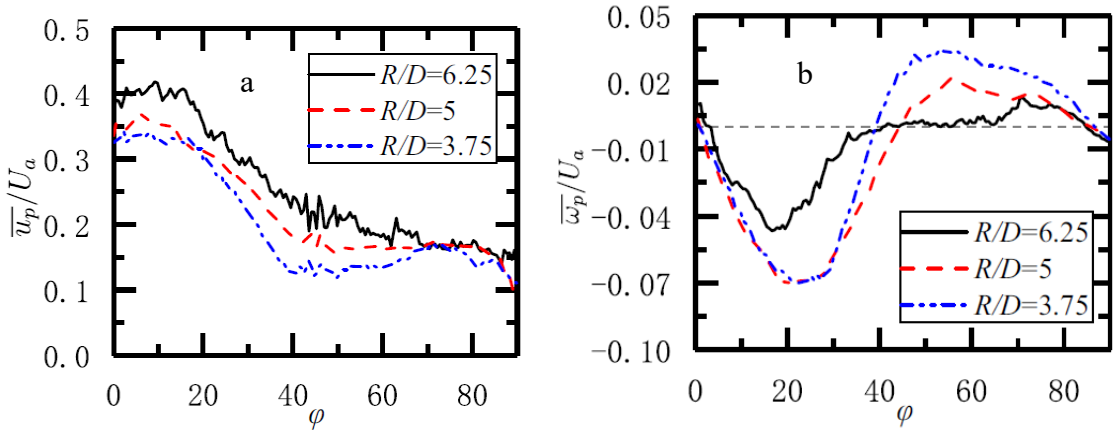

Figure 3.8: (a) normalized averaged axial particle velocity, (b) normalized averaged radial particle velocity from Fei et al.[1] modified

3.5 Pressure Drops at first bend

Rui et al. [36] executed experiments on the same apparatus described in Fei et al. [6] with exactly the same particles, characterized in Section 3.2 to investigate the pressure drops at the first bend and develop a correlation. The simulated first bend pressure drops, obtained in all the frameworks evaluated, are then compared with the correlation.

$$\begin{cases} \mathrm{Re} = \dfrac{\rho_f \mathbf{u}_f D}{\mu_f} \\ m_s = \dfrac{G_s}{\rho_f \mathbf{u}_f A} \\ \Delta p_{bend} = \left(\dfrac{4.452}{\mathrm{Re}^{0.593}} \left(6.55 \left(\dfrac{R}{D} \right)^{1.25} + \dfrac{88.66}{\left(R/D \right)^{1.25}} \right) + \dfrac{1.353 m_s^{0.85}}{\mathrm{Re}^{0.13} \left(R/D \right)^{0.882}} \right) \dfrac{\rho_f \mathbf{u}_f^2}{2} \end{cases} \tag{3.2}$$

3.6 Simulations' Geometry

The geometry employed to perform all the simulations is generated with the software CATIAV5, then the suitable format is chosen to export it in BarracudaVR, which uses extension. stl, and Ansys Fluent, which uses extension. igs. In Fig. 5.1 is shown a frontal view of the 3D geometry that has been created: the hooper, present in the experimental work, has been deleted, as that part would not have contributed to the accuracy of the results. Moreover, being quite big, including this part in the geometry would results in augmenting the number of computational cells presents in the system increasing the computational time required to perform calculations, besides complicating the mesh generation process. This part of the geometry is replaced by a line dedicated to solid feeding, along with solid a small air flowrate is fed, to avoid numerical problems, especially when the particles are described with a Lagrangian frameworks. Because of this change it is imposed that, when the particles reach the outlet of the pneumatic conveying line, they simply exit the systems, while particles are fed in continuous from the particle feeding pipe. As the experiments are performed with three different values of R/D, three different geometries are created, with the selected R/D ratio, keeping the other geometrical constraints at the value indicated by the article.

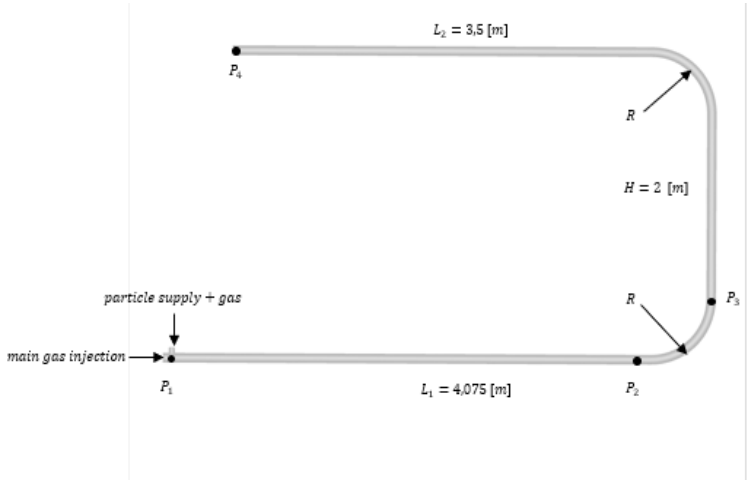

Figure 5.1: geometry realized in CATIAV5

3.7 Procedure

The simulations in all the frameworks assessed are conducted in transient, with a timestep equals to 0.0001 [s]. The configuration characterized by R/D equals to 6.25 and superficial air velocity equals to 17 [m/s] is taken as reference for the first part of the study, which consists of finding the parameters settings which ensure convergency, starting from the default ones. At the same time, by comparing the inlet and the outlet solid flowrate, evaluating the simulation time at which a SteadyState condition is reached. Subsequently, the simulations are carried one for one second longer in comparison to that one needed to reach the SteadyState; to obtain though the last second, time averaged quantities of interest. The conveying line ΔP are taken as reference parameter to perform a mesh independence study and find the proper mesh refining degree. After that, with the same configuration, a sensitivity analysis is made to study the influence of the parameters, and a tuning, keeping the line *ΔP* as reference parameter. Subsequently, when possible, the influence of drag model choice is evaluated, comparing the particles' velocity axial and radial component at the first bend and the line *ΔP* varying this time the superficial air velocity with respect to the results obtained in

the article. Finally, with the selected parameters and drag model, all the configurations are evaluated, and all the results are compared with that of the article. Moreover, the predicted bend pressure drops of the simulation are compared with a correlation developed by Fei et al.[36] .

The line pressure drops are obtained subtracting the pressure value at the air inlet section with that of the outlet of the conveying line, these two surfaces are defined also to set the boundary condition.

Following the article, the particles' velocity is obtained through a plane, inclined of an angle φ with respect to the direction of the gravity, passing across the bend axis. To mimic this in all the CFD codes employed, ten surface lines are created, one every 10° of φ, and the velocities through those are obtained. The surface lines are created starting from one point at the outer wall of the pipe and one at the inner, imposing that the straight line passing through those points pass across the center of the bend. All the CFD codes used employ a cartesian reference system, showed in Fig.5.2, whose origin is placed at the center of the main conveying pipe inlet section.

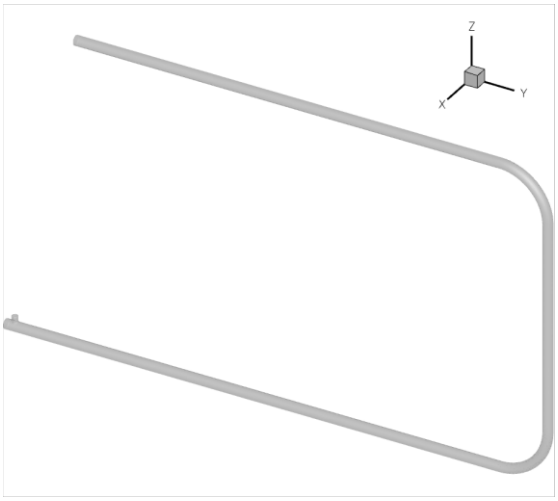

Figure 5.2: 3D geometry and reference system

With respected to the reference system the coordinates of the bend center are:

$$\begin{cases} x=0 \\ y=y0 \\ z=R \end{cases} \tag{3.3}$$

Where R is the bend radius, and y_0 the length of the first horizontal trait. Considering the reference system pictured in fig.5.2, a generic point belonging to the inner wall:

$$\begin{cases} x = 0 \\ y = y_0 + \left(R - \frac{D}{2} \right) \sin\theta \\ z = z_0 - \left(R - \frac{D}{2} \right) \cos\theta \end{cases} \tag{3.4}$$

Where D is the pipe diameter, y_0 the length of the first horizontal trait, and z_0 equal to the bend radius R. Similarly, a point of the outer wall has coordinates:

$$\begin{cases} x = 0 \\ y = y_0 + \left(R + \dfrac{D}{2} \right) \sin\theta \\ z = z_0 - \left(R + \dfrac{D}{2} \right) \cos\theta \end{cases} \tag{3.5}$$

It must be underlined the CFD codes employed can supply the particles' velocity components along the reference frame described above, while to compare the results it is necessary to obtain the radial and axial components. This can be done as:

$$\begin{cases} \omega_p = v_z \cos\varphi - v_y \sin\varphi \\ u_p = v_z \sin\varphi + v_y \sin\varphi \end{cases} \tag{3.6}$$

Where u_p is the axial part and ω_p the radial one.

4. Multiphase Modelling

Pneumatic conveying is an industrial application that falls into classification of multiphase flow, as it is a gas-solid system. In general, multiphase flows are classified in terms of separated, as in the case of immiscible liquids, in which all the phases are continuous, or dispersed systems, where there is one continuous phase, and another is present in the form of particles or droplets. In turn, dispersed systems can be dense or dilute, depending on the spacing between the entities that constitutes the particles or droplets. To simulate the case study are employed the multiphase models Euler-Euler, Euler-Lagrangian, and Multiphase-Particle-in-cell.

4.1 Multiphase Particle-in-cell Model

The multiphase particle-in-cell (MP-PIC) is a method that models the fluid phase present in the simulation as a continuum, using a Eulerian model, and, for the particles, implements a mixed Eulerian-Lagrangian description, Snider at al. [12]. This model has been developed to overcome the weak points of previously developed models as Euler-Euler two fluid model and Lagrangian-Eulerian model. In Eulerian-Eulerian models both the solid and the fluid phase are treated as interpenetrating continua, allowing to model the particle-particle stresses, but, when a particle size distribution is introduced, many equations are required to be solved, increasing the computational cost. In the Lagrangian-Eulerian model instead, the fluid phase is treated as a continuum, while the solid phase is described as discrete, nevertheless when the particle volume fraction rises above 5% the particles' collision frequency becomes too high to be efficiently modeled. The continuity equation for the fluid phase when mass transfer is null, is expressed as:

$$\frac{\partial\left(\theta_f \rho_f\right)}{\partial t} + \nabla_x \cdot \left(\theta_f \rho_f \mathbf{u}_f\right) = 0 \tag{4.1}$$

Where θ_f is the fluid volume fraction, ρ_f is the fluid density and $\mathbf{u_f}$ the fluid velocity. The momentum equation for the fluid phase is:

$$\frac{\partial\left(\theta_f \rho_f \mathbf{u}_f\right)}{\partial t} + \nabla \cdot \left(\theta_f \rho_f \mathbf{u}_f \mathbf{u}_f\right) = -\nabla p - \mathbf{F} + \theta_f \rho_f \mathbf{g} \tag{4.2}$$

Where **F** is the interphase drag force between the fluid and solid phase, expressed as:

$$\mathbf{F} = \iint \phi m \left[D\left(\mathbf{u}_f - \mathbf{u}_p\right) - \frac{1}{\rho_p} \nabla p \right] dm d\mathbf{v} \tag{4.3}$$

Where m is the solid mass, $\mathbf{u_p}$ the particle velocity, ρ_p the solid density, **p** the pressure and ϕ the particle radial distribution function.

The particles evolution is modeled through a Liouville equation that considers the particle distribution function ϕ (**x**, $\mathbf{u}_\mathrm{p}$, ρ_p, m, t) which depends to particle position **x**, velocity, density, and mass:

$$\frac{\partial\left(\phi\right)}{\partial t} + \nabla_x \cdot \left(\phi \mathbf{u}_p\right) + \nabla_{u_p} \cdot \left(\phi \mathbf{A}\right) = 0 \tag{4.4}$$

Where **A** is the particle acceleration, expressed as:

$$\mathbf{A} = D\left(\mathbf{u}_f - \mathbf{u}_p\right) - \frac{1}{\rho_p} \nabla_x p + \mathbf{g} - \frac{1}{\theta_p \rho_p} \nabla_x \tau \tag{4.5}$$

Where D is the drag function and τ is the isotropic solid stress, both will be further described in the parameters model section, while θ_p is the particle volume fraction:

$$\theta_p = \iint \phi m \left[D\left(\mathbf{u}_f - \mathbf{u}_p\right) - \frac{1}{\rho_s}\nabla p \right] dm d\mathbf{u}_p \tag{4.6}$$

The particle volume fraction is linked to the particle volume fraction with the relationship:

$$\theta_f + \theta_p = 1 \tag{4.7}$$

Multiplying the eq. (4.4) by m and $m\mathbf{u}_p$ and integrating over mass and velocity are obtained the conservation equation, in particular the particle continuity equation is:

$$\frac{\partial\left(\theta_p \rho_p\right)}{\partial t} + \nabla_x \cdot \left(\theta_p \rho_p \mathbf{u}_p\right) = 0 \tag{4.8}$$

And the particle momentum equation is:

$$\begin{aligned} &\frac{\partial\left(\theta_p \rho_p \mathbf{u}_s\right)}{\partial t} + \nabla_x \cdot \left(\theta_p \rho_p \mathbf{u}_s\right) + \nabla_x \tau + \theta_p \nabla_x p = \\ &\theta_p \rho_p \mathbf{g} + \iint \phi m D\left(\mathbf{u}_f - \mathbf{u}_p\right) dm d\mathbf{u}_p - \nabla_x \cdot \left[\iint \phi m \left(\mathbf{u}_p - \mathbf{u}_s\right)\left(\mathbf{u}_p - \mathbf{u}_s\right) dm d\mathbf{u}_p \right] \end{aligned} \tag{4.9}$$

Where $\mathbf{u}_s$ is the mean particle velocity, expressed as:

$$\mathbf{u}_s = \frac{1}{\theta_p \rho_p} \iint \phi m \mathbf{u}_p dm d\mathbf{u}_p \tag{4.10}$$

In this framework particles are grouped in entities named parcel or computational clouds, inside which all particles have the same characteristic in terms of velocity, volume, and density. As the parcel travel the domain the number of particles inside each cloud remains constant and so each parcel does not exchange mass with the domain, this conservation principle is expressed mathematically with eq. (4.4). The software solves the equation for parcels to reduce the computational time, by implementing a finite difference approximation, the fluid phase equations instead are solved with a finite volume approximation.

4.1.1 Model parameters

The isotropic interparticle stress, is a tensor with off-diagonal null elements, derived starting from the particle stress model employed is based on Snider et al.[12], which is an extension of the model developed by Harris et al.[14], is computed as :

$$\tau = \frac{P_s \theta_p^{\ \beta}}{\max\left[\theta_{cp} - \theta_p, \varepsilon\left(1 - \theta_p\right)\right]} \tag{4.10}$$

Where P_s is a constant with the unit of a pressure, β is a constant for which Auzerais et al. [16] set the recommended interval as $2 \leq \beta \leq 5$ and ε is set at 10^{-7} and θ_{cp} is the close pack particle volume fraction, defined as:

$$\theta_{cp} = \frac{\rho_{bulk}}{\rho_p} \tag{4.11}$$

In Fig. 4.1 the isotropic interparticle stress is showed as function of the particle volume fraction: one should note that the particles are affected by the isotropic interparticle stress

only in regions where the particle volume fraction approaches the close-pack limit. In this way, particles approaching regions where the particle volume fraction is near the close-pack limit would be redispersed according to their solid stress tensor and incidence angle and the parameter “maximum momentum redirection from collision,” customizable by the user.

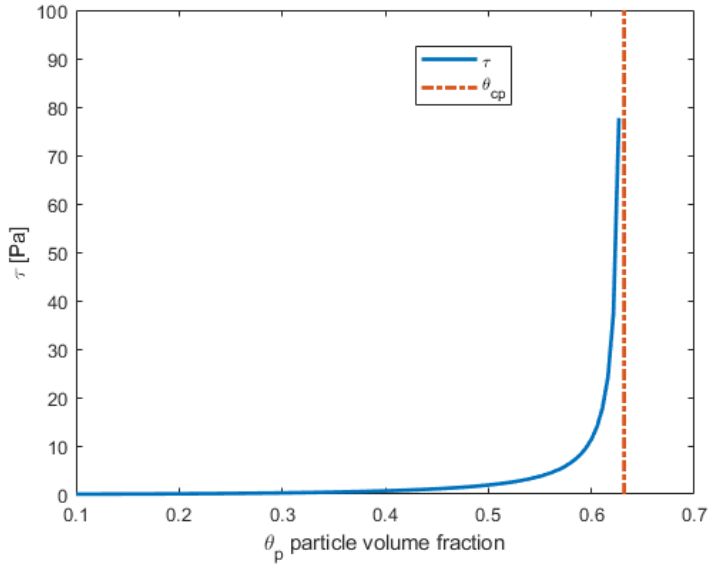

Figure 4.1: isotropic particle stress

The fraction of tangential and normal momentum, maintained by the particles after the collision with the wall, is expressed by two constant values, adjustable by the user, and set at 0.85 by default. Fig.4.2 shows a scheme of particle to wall collision, where n is the time preceding the collision and n+1 the time behind.

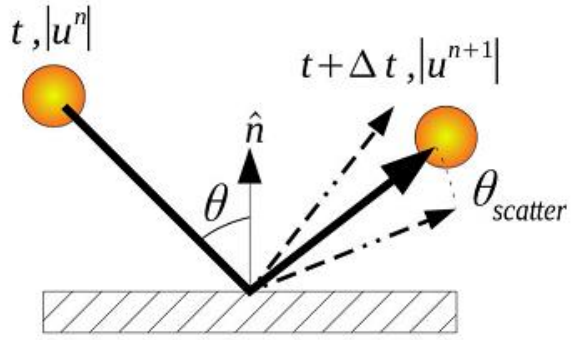

Figure 4.2: particle collision with the wall

The relationship between the velocities u^n and u^{n+1} is:

$$\left|\mathbf{u}^{n+1}\right| = \left[\left(r_T - r_N\right)\left(1-\cos\theta\right) + r_N\right]\left|\mathbf{u}^{n}\right| \tag{4.12}$$

Where r_T and r_N are respectively the tangent and the normal particle momentum retention. One should note that, when the particle velocity vector is perpendicularly to the wall, only the normal particle momentum retention affects the particle velocity after the collision.

To model the change on angle θ, formed between the particle velocity vector and the normal to wall and showed in Fig.4.2, after the particle collision with the wall, a diffuse bounce coefficient is introduced. The changing on this angle is due to the shape of the particles, which are not perfectly spherical, and the roughness of the wall introducing a stochastic changing to θ. This coefficient ranges from 0 to 5, where 5 corresponds to maximum possible stochastic variation in angle θ and is the most computational expensive option.

As previously explained in the MP-PIC model the equations of motion for the solid phase are solved for the computational clouds, or parcels, in which particles with the same characteristics are grouped. The user, in the boundary condition panel, can specify the manual density number, computed as:

$$n_p = \frac{N_p}{N_{cells}\theta_p} \tag{4.12}$$

Where n_p is the manual density number, N_{cells} is the total number of cells in the computational grid and θ_p is the particle volume fraction. To obtain results that are statistically representative of the particles' behavior the manual density number should be set in such a way that, once the simulation has reached the steady state, the ratio between the computational parcels and the total number of cells is bigger than 10, Smagorinski et al. [15]. It must be underlined that increasing the value of this parameter augments the computational time, so a compromise must be found.

The interphase drag models are implemented to obtain the drag coefficient C_{d} starting from which is possible to compute the drag function D, present in eq. (4.3) and (4.9) through:

$$D = \frac{3}{4} C_d \frac{\rho_f \left|\mathbf{u}_f - \mathbf{u}_p\right|}{\rho_p d_p} \tag{4.13}$$

Where d_p is the particle diameter. The drag models included in BarracudaVR that can be applied to describe the dilute phase pneumatic conveying, in all of them appears the particle Reynolds number:

$$\mathrm{Re} = \frac{d_p \left|\mathbf{u}_f - \mathbf{u}_p\right|}{\nu_f} \tag{4.14}$$

Where ν_f is the fluid kinematic viscosity. To simulate the dilute phase pneumatic conveying case study three drag laws are taken into consideration: Wen-Yu, developed for dilute-phase system, and non-spherical Ganser. The Wen-Yu model [18] has the form:

$$C_d = \begin{cases} \dfrac{24}{\mathrm{Re}}\theta_f^{-2.65} & \mathrm{Re} < 0.5 \\ \dfrac{24}{\mathrm{Re}}\theta_f^{-2.65}\left(1 + 0.173\,\mathrm{Re}^{0.657}\right) & 0.5 \le \mathrm{Re} \le 1000 \\ 0.44\,\theta_f^{-2.65} & \mathrm{Re} > 1000 \end{cases} \tag{4.15}$$

The non-spherical Ganser drag model has the form:

$$C_d = \theta_f^{-2.65} K_2 \left[\frac{24}{\mathrm{Re}\, K_1 K_2} \left(1 + 0.11 \left(\mathrm{Re}\, K_1 K_2\right)^{0.66}\right) + \frac{0.43}{1 + \frac{3305}{\mathrm{Re}\, K_1 K_2}} \right] \tag{4.16}$$

Where K_1 and K_2 are:

$$K_1 = \frac{3}{1+2\psi^{-0.5}} \qquad K_2 = 10^{1.81\left(-\log\psi\right)^{0.57}} \tag{4.17}$$

4.2 Two Fluid Model

The two fluid model (TFM) is a Eulerian-Eulerian model in which all the phases are treated as interpenetrating continua, and for each of them the continuity and momentum equation are solved [19] and a unique value of pressure is shared. To describe the phases as interpenetrating continua, the phase volume fraction is introduced:

$$V_q = \int_V \theta_q \, dV \tag{4.18}$$

Where for the θ_q is the phase volume fraction:

$$\sum_{q=1}^{n} \theta_q = 1 \tag{4.19}$$

The continuity equation for the fluid when mass transfer is null, is expressed as:

$$\frac{\partial\left(\theta_f \rho_f\right)}{\partial t} + \nabla_x \cdot \left(\theta_f \rho_f \mathbf{u}_f\right) = 0 \tag{4.20}$$

Where θ_f is the fluid volume fraction, ρ_f is the fluid density and $\mathbf{u}_f$ the fluid velocity. The momentum equation for the fluid phase is:

$$\frac{\partial\left(\theta_f \mathbf{u}_f \rho_f\right)}{\partial t} + \nabla \cdot \left(\theta_f \rho_f \mathbf{u}_f \mathbf{u}_f\right) = -\theta_f \nabla p + \nabla \tau_f + \theta_f \rho_f \mathbf{g} + K_{fp}\left(\mathbf{u}_p - \mathbf{u}_f\right) \tag{4.21}$$

Where p is the pressure shared by all phases, $\mathbf{u}_\mathrm{f}$ the fluid phase velocity, $\mathbf{u}_\mathrm{p}$ the particle phase velocity and K_{fp} the interphase drag coefficient, which will be further described in the next section. For the fluid phase stress tensor, a Newtonian behavior is assumed:

$$\tau_f = \theta_f \rho_f \left(\nabla \mathbf{u}_f + \nabla \mathbf{u}_f^T\right) + \theta_f \left(\lambda_f - \frac{2}{3}\mu_f\right) \nabla \mathbf{u}_f \mathrm{I} \tag{4.22}$$

Where μ_f and λ_f are respectively the shear and bulk viscosities. Similarly, to the fluid phase, the solid phase is described as a continuum, the continuity equation is expressed as:

$$\frac{\partial\left(\theta_p \rho_p\right)}{\partial t} + \nabla_x \cdot \left(\theta_p \rho_p \mathbf{u}_f\right) = 0 \tag{4.23}$$

Where θ_p is the particle volume fraction, ρ_p the particle density and $\mathbf{u}_p$ the particle velocity. The momentum equation is:

$$\frac{\partial\left(\theta_p \rho_p \mathbf{u}_p\right)}{\partial t} + \nabla \cdot \left(\theta_p \rho_p \mathbf{u}_p \mathbf{u}_p\right) = -\theta_p \nabla p - \nabla p_s + \nabla \tau_s + \theta_p \rho_p \mathbf{g} + K_{fp}\left(\mathbf{u}_f - \mathbf{u}_p\right) \tag{4.24}$$

Where p_s is the solid pressure and τ_s. The solid stress tensor is written in the form of the fluid stress tensor, assuming a Newtonian strain-rate behavior:

$$\tau_s = \theta_p \rho_p \left(\nabla \mathbf{u}_p + \nabla \mathbf{u}_p^T \right) + \theta_p \left(\lambda_s - \frac{2}{3} \mu_s \right) \nabla \mathbf{u}_p \mathrm{I} \tag{4.25}$$

Where μ_s and λ_s are respectively the shear and bulk solid viscosities and will be further described.

4.2.1 TFM parameters

To obtain the fluid-solid exchange coefficient K_{fp} the particle Reynolds number Re_s must be defined:

$$\mathrm{Re}_s = \frac{\rho_f d_p \left| \mathbf{u}_p - \mathbf{u}_f \right|}{\mu_f} \tag{4.26}$$

For the description of dilute phase pneumatic conveying, it is possible to apply the Syamlal and O'Brien drag model in which the drag function is obtained from Dalla Valle [22]:

$$C_D = \left(0.63 + \frac{4.8}{\sqrt{\mathrm{Re}_s / v_{r,s}}} \right)^2 \tag{4.27}$$

Where v_{rs} is the terminal velocity of a particle for the solid phase, from Garside [24] as:

$$v_{r,s} = 0.5 \left(A - 0.06 \mathrm{Re}_s + \sqrt{\left(0.06 \mathrm{Re}_s \right)^2 + 0.12 \mathrm{Re}_s \left(2B - A \right) + A^2} \right) \tag{4.28}$$

Where:

$$\begin{cases} A = \theta_f^{4.14} \\ B = 0.8 \theta_f^{1.28} & \theta_f \le 0.85 \\ B = \theta_f^{2.65} & \theta_f > 0.85 \end{cases} \tag{4.29}$$

Finally, the fluid-solid exchange coefficient K_{fp}:

$$K_{fp} = \frac{3 \theta_p \theta_f \rho_f}{4 v_{r,s}^2 d_p} C_D \left(\frac{\mathrm{Re}_s}{v_{r,s}} \right) \left| \mathbf{u}_p - \mathbf{u}_f \right| \tag{4.30}$$

Another drag model which suits the problem in exam is that of Wen-Yu, which has been described in Section 4.1.4 .

A solids pressure terms is introduced considering the additional normal stress due to the particles' collisions in a compressible regime. This term is constituted by a collision and a kinetic term, from Lun et al. [26]:

$$p_s = \theta_p \rho_p \Theta_s + 2 \rho_P \left(1 + e_{ss} \right) \theta_p^2 g_{0,ss} \Theta_s \tag{4.31}$$

Where Θ_s is the granular temperature, $g_{0,ss}$ the radial distribution function and e_{ss} the coefficient of restitution, that considers the nature of particles' collisions. A fully elastic collision occurs when this parameter is unitary, while a fully inelastic when it is null.

The granular Temperature is obtained through a transport equation derived from the kinetic theory of granular flow, developed by Gidaspow [27] which makes a parallelism between the kinetic theory of a granular phase with that one of dense gases. In the algebraic formulation, convection ad diffusion terms are neglected, the transport equation reduces to:

$$\frac{3}{2}\left[\frac{\partial\left(\theta_p\rho_p\Theta_s\right)}{\partial t}\right]=\left(-p_s\mathbf{I}+\tau_s\right):\nabla\mathbf{u}_p-\gamma_{\Theta_s}+\phi_{fp} \tag{4.32}$$

Where $\gamma_{\Theta s}$ is the energy dissipation rate due to particle collisions from Lun et alt [23]:

$$\gamma_{\Theta_s}=\frac{12\left(1-e_{ss}^2\right)g_{0,ss}}{d_p\sqrt{\pi}}\rho_p\theta_p^2\Theta_s^{3/2} \tag{4.33}$$

The term ϕ_{fp} represents the kinetic energy transfer, from the solid to the fluid phase, due to fluctuations in particle velocity field from Gidaspow et al. [28]:

$$\phi_{fp}=-3K_{fp}\Theta_s \tag{4.34}$$

In the solid stress tensor shear and bulk viscosity appear. The first term is written as the sum of collisional and a kinetic viscosity term, as the frictional part in a dilute phase system is normally neglected:

$$\mu_s=\mu_{s,col}+\mu_{s,kin} \tag{4.35}$$

The collisional part is computed from Lun et al. [26]:

$$\mu_{s,col}=\frac{4}{5}\theta_p\rho_p d_p g_{0,ss}\left(1+e_{ss}\right)\left(\frac{\Theta_s}{\pi}\right)^{1/2}\theta_p \tag{4.36}$$

The kinetic part, in a dilute phase system, is obtained by Syamlal et al. [29]

$$\mu_{s,kin}=\frac{\theta_p d_p\sqrt{\Theta_s\pi}}{6\left(3-e_{ss}\right)}\left[1+\frac{2}{5}\left(1+e_{ss}\right)\left(3e_{ss}-1\right)\theta_p g_{0,ss}\right] \tag{4.37}$$

The bulk viscosity is obtained from Lun et al. [26]:

$$\lambda_s=\frac{4}{3}\theta_p\rho_p d_p g_{0,ss}\left(1+e_{ss}\right)\left(\frac{\Theta_s}{\pi}\right)^{1/2} \tag{4.38}$$

The radial distribution function is a dimensionless parameter that expresses the mean distance between the particles that constitutes the granular flow. In the study case, as only one solid phase is present, it is obtained from Ogawa et al. [30]:

$$g_{0,ss}=\left[1-\left(\frac{\theta_p}{\theta_{p,\max}}\right)^{1/3}\right]^{-1} \tag{4.39}$$

Where $\theta_{p,max}$ is the maximum packing limit. If only one solid phase is present, with a unique diameter, is a constant fixed by default at 0.63.

The specularity coefficient φ is an empirical parameter specifies the roughness or the smoothness of the wall, and so the nature of particle wall collisions: when φ=0 is equivalent to perfectly smooth wall, while φ=1 is equivalent to impose maximum roughness. When the Johnson and Jackson boundary conditions [29] at the wall are applied, φ=1 provides the same results as the no slip condition. Those boundary conditions are:

$$\begin{cases} S=-\dfrac{\pi}{6}\sqrt{3}\varphi\dfrac{\theta_p}{\theta_{p,\max}}\rho_p g_{0,ss}\sqrt{\Theta_s}\mathbf{u}_{s/} \\ -n\cdot q=-S\mathbf{u}_{s/}+\dfrac{\pi}{4}\sqrt{3}\dfrac{\theta_p}{\theta_{p,\max}}\rho_p g_{0,ss}\left(1-e_{ss}^2\right)\Theta_s^{3/2} \end{cases} \tag{4.40}$$

Where S is the tangential solid shear stress and q the flux of fluctuation energy at a flat frictional wall.

4.3 Discrete Phase Model

The discrete phase model (DPM) is a Eulerian-Lagrangian framework where the fluid phase is treated as a continuum, as it is modeled with the Navier-Stokes equation, while the second Newton's law is applied to computational clouds, ensemble of particles that constitutes the dispersed phase. According to Elgobashi et al.[33] there are three diverse ways to describe the interaction between the discrete and the continuous phase: one-way coupling, two-way coupling or four-way coupling. In the one-way coupling the continuous phase impacts the dispersed one, on the contrary the dispersed one does not affect the flow field of the continuous one. In the two-way coupling both phases affect each other, but the particle-particle interactions are not modeled, while in the four-way coupling also interparticle interactions are included. In this work, as the system operates in dilute phase regime and modeling interparticle interactions is expensive computationally speaking, all the simulations are conducted with a two-way coupling framework. In the point-particle approach, the fluid flow is solved with a modified version of the Navier-Stokes equations, which includes particle source terms:

$$\frac{\partial\left(\theta_f \rho_f\right)}{\partial t} + \nabla_x \cdot \left(\theta_f \rho_f \mathbf{u}_f\right) = Sc \tag{4.41}$$

$$\frac{\partial\left(\theta_f \mathbf{u}_f \rho_f\right)}{\partial t} + \nabla \cdot \left(\theta_f \rho_f \mathbf{u}_f \mathbf{u}_f\right) = -\theta_f \nabla p + \nabla \tau_f + S_{i,p} \tag{4.42}$$

Where S_C and $S_{i,p}$ represents respectively the mass and momentum transfer between the particles and the fluid. To track the computational clouds the second Newton's law is employed, where in the study-case, it is written as:

$$m_d \frac{du_{i,p}}{dt} = F_{drag} \tag{4.43}$$

Where F_{drag} is the drag force acting on a computational cloud, which is given by:

$$F_{drag} = \frac{1}{2} A_d C_D \rho_f \left|\mathbf{u}_f - \mathbf{u}_p\right|\left(\mathbf{u}_f - \mathbf{u}_p\right) \tag{4.44}$$

Where A_d is the particle projected area in the direction of the flow. As the particle are not spherical, in this framework the drag coefficient C_d is calculated with the non-spherical Haider-Levenspiel model [18]:

$$C_d = \theta_f^{-2.65}\left[\frac{24}{\mathrm{Re}}\left(1 + 8.2\,e^{-4.07\psi}\,\mathrm{Re}^{\left(0.01+0.56\psi\right)}\right)\right] + \frac{72e^{-5.07\psi}\,\mathrm{Re}}{\mathrm{Re} + 5.4\,e^{6.2\psi}} \tag{4.45}$$

The parameters that most affect this model are the particle-wall interactions, described in section (4.1) which are defined in this framework in the same fashion.

4.4 Turbulent Models

As the pneumatic conveying operation occurs at high superficial gas velocities, the convective transport term of the Navier-Stokes equations cannot be neglected, and a model is required to accurately describe the dynamic of the system.

In direct numerical simulation the Navier-Stokes equations are directly solved without a model the turbulence. To capture the features pf the turbulence, time and spatial scale must be of the order of magnitude of the smallest Kolmogorov timescale τ_η and length scale η:

$$\eta = \left(\frac{\nu^3}{\varepsilon} \right)^{1/4} \tag{4.46}$$

$$\tau_\eta = \left(\frac{\nu}{\varepsilon} \right)^{1/2} \tag{4.47}$$

Where ν is the fluid kinematic viscosity and ε the energy dissipation rate. As this model is extremely computational expensive, is not feasible for engineering application.

In Large eddy simulation (LES) the smallest time and spatial scales are unsolved. This is motivated to the nature of the eddies at smallest scales, which are isotropic and easy to model, in contrast to the larger ones which are anisotropic and so difficult to compute. The effect of the smallest eddies is modeled introducing subgrid stress and subsequent a subgrid viscosity.

The Reynolds decomposition approach [34] consists of splitting an instantaneous variable into a mean and a fluctuating part, due to turbulence, this operation is applied to the Navier-Stokes equations :

$$\nabla\left(\mathbf{u} + \langle \mathbf{u} \rangle\right) = 0 \tag{4.48}$$

$$\frac{\partial\left(\langle \mathbf{u} \rangle + \mathbf{u}\right)}{\partial t} + \left(\left(\langle \mathbf{u} \rangle + \mathbf{u}\right) \cdot \nabla\right)\left(\langle \mathbf{u} \rangle + \mathbf{u}\right) = -\frac{1}{\rho}\nabla\left(\langle P \rangle + P\right) + \nu \nabla^2 \left(\langle \mathbf{u} \rangle + \mathbf{u}\right) \tag{4.49}$$

Subsequently an integral averaging over time, where the integration time must be bigger in comparison to the timescale of turbulence, but smaller in comparison to that of the mean value, is applied to the Navier-Stokes equations, to isolate the part related to turbulent fluctuations from the one due to mean values. In this way the Reynolds Averaging Navier-Stokes (RANS) equations are obtained:

$$\nabla \langle \mathbf{u} \rangle = 0 \tag{4.50}$$

$$\frac{\partial \langle \mathbf{u} \rangle}{\partial t} + \langle \mathbf{u} \rangle \nabla \cdot \langle \mathbf{u} \rangle = -\frac{1}{\rho}\nabla \langle P \rangle + \nu \nabla^2 \langle \mathbf{u} \rangle - \nabla \langle \mathbf{u} \cdot \mathbf{u} \rangle \tag{4.51}$$

The equation (4.51) contains in the last term of the right-hand side the product of the velocity fluctuations, named Reynold stress tensor that requires a closure model. The Boussinesq approximation models the transport of momentum due to turbulence in the form of a diffusive process, with a turbulent or eddy viscosity ν_T:

$$-\nabla \langle \mathbf{u} \cdot \mathbf{u} \rangle = \nu_T \left(\nabla \langle \mathbf{u} \rangle + \nabla \langle \mathbf{u} \rangle^T \right) - \frac{2}{3} k \mathbf{I} \tag{4.52}$$

The turbulent viscosity ν_T is obtained as:

$$\nu_T = C_v u l \tag{4.53}$$

Where u and l are respectively the characteristic velocity and length scale for the large turbulent eddies, and C_v is a proportionally constant. As ν_T can vary in space and time, a turbulence model that supplies further equations to close the set of equations. Depending on the number of further equations introduced, a model can be classified in zero, one and two-equation model. The most often used are the two-equations models in which one equation solves for the turbulent velocity scale k and another for a further turbulent property ϕ which can be expressed as:

$$\phi = k^{\alpha} l^{\beta} \tag{4.54}$$

In Tab. 4.1 the most popular values for α and β are reported:

Table 4.1. Commonly used properties to find l from Andersson [19] modified

α	β	ϕ	Symbol of ϕ
0	1	l	l
1	-2	k/l^2	ω
1/2	-1	$k^{1/2}/l$	f
-1/2	1	$k^{-1/2}/l$	τ
3/2	-1	$k^{3/2}/l$	ε

The most employed models are the k-ε models, where the property ϕ is the dissipation rate ε. There are three different the k-ε models: the standard k-ε, RNG k-ε and Realizable k-ε, in this work the standard k-ε model with has been employed for the DPM-two way coupling framework, while the standard k-ε dispersed model has been employed for the Euler-Euler two fluid model framework. In both cases a standard wall function has been used.

The k-ε standard model is popular as ensures a good accuracy, especially for flows characterized by high Re, with low computational cost. As previously written this model introduces two additional equations to the original Navier-Stokes equations, to solve for the turbulent kinetic energy k and the energy dissipation rate ε. Inside these two additional transport equations several terms are unknown and some closures, based on assumptions, are required to solve these equations, which, in their final form, are written as:

$$\frac{\partial k}{\partial t} + \nabla \cdot \left(\langle \mathbf{u} \rangle k \right) = \nu_T \left[\left(\nabla \langle \mathbf{u} \rangle + \nabla \langle \mathbf{u} \rangle^T \right) \nabla \langle \mathbf{u} \rangle \right] - \varepsilon + \nabla \left[\left(\nu + \frac{\nu_T}{\sigma_k} \right) \nabla k \right] \tag{4.55}$$

$$\frac{\partial \varepsilon}{\partial t} + \nabla \cdot \left(\langle \mathbf{u} \rangle \varepsilon \right) = C_{\varepsilon 1} \nu_T \frac{\varepsilon}{k} \left[\left(\nabla \langle \mathbf{u} \rangle + \nabla \langle \mathbf{u} \rangle^T \right) \nabla \langle \mathbf{u} \rangle \right] - C_{\varepsilon 2} \frac{\varepsilon^2}{k} + \nabla \left[\left(\nu + \frac{\nu_T}{\sigma_k} \right) \nabla \varepsilon \right] \tag{4.56}$$

5. Multiphase particle-in-cell

The MP-PIC method was implemented in BarracudaVR 21.1.0 software developed by the company CPFD.

5.1 Mesh generation process

Creating a proper mesh is a crucial point in CFD simulations, as it can affects dramatically the accuracy of the results. To create a computational grid on BarracudaVR, the first step is to import the geometry CAD file, which must be in. stl format, and selecting the proper units in which the software must read the file, in this case [mm]. Once the geometry has been imported a cartesian refence system, whose origin is located at the middle of the lower horizontal tube, is automatically generated. Subsequently one must place in correctly the grid lines in the imported geometry as depicted below. In BarracudaVR three types of grid lines are present: the major grid lines, depicted in Fig. 5.1 in black, are used to capture key features of the imported geometry and are found at fixed positions

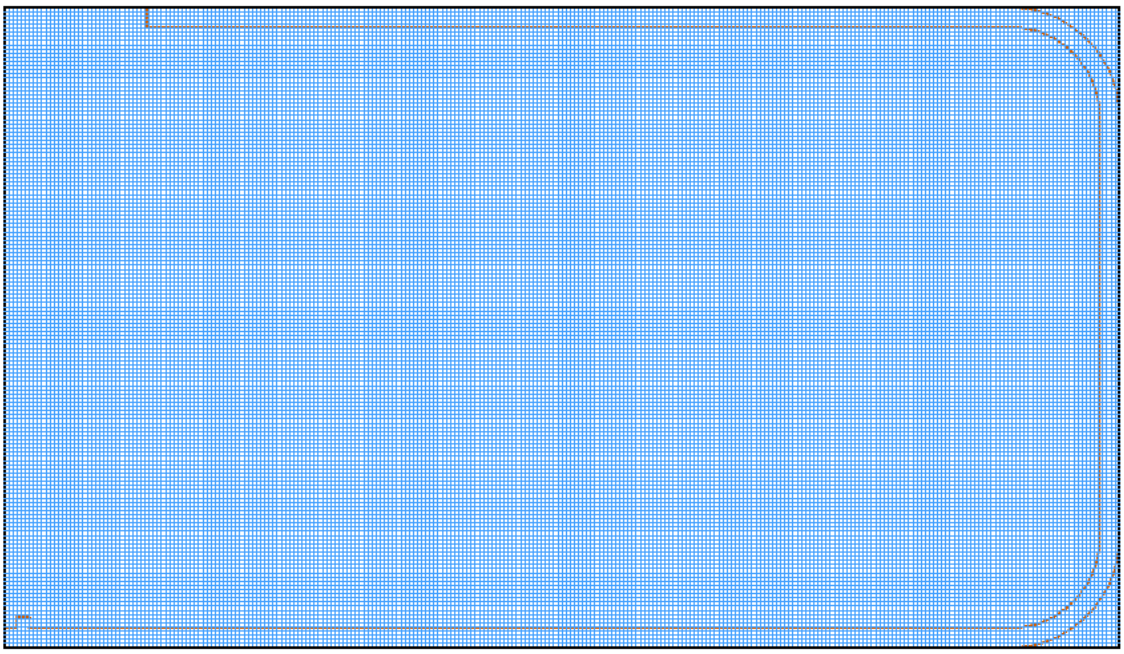

Figure 5.1: yz plane view of BarracudaVR geometry and grid lines

The minor grid lines, shown in blue in Fig.5.1, which are evenly spaced between the major grid lines, and can be used to increase the grid resolution. Finally, the non-linear grid lines, which are not shown, are used if in the computational domain there is a region with more refined cells in contact with a region with coarser ones, to favor a smooth transition. Once the major grid lines have been placed, selecting their coordinates to completely enclose the geometry of interest, the grid was created by using the panel “setting a uniform grid,” choosing the desired total number of cells value. Entering this value, the software will generate the proper number of equispaced minor grid lines that will assure the desired value of total cells enclosed between the major grid line. The effective computational grid is generated by the grid generator tool by finding the region of space inside the stl geometry file, depicted in Fig.5.1 in red, and creating cells inside it. To create the boundary walls, the grid generator will look for intersections between the wall of stl geometry and the grid lines, those

intersections will be treated with the same priority. The computational cells found at the boundary are treated with a cut-cell method, to make sure that the domain will follow the shape of the geometry of interest. The main issue related to this method is that small cells are created at the boundary, and this can create numerical problems, as the particles will not move smoothly inside the cells. To solve this issue there are two practical options: “remove small cells only” and “merge and remove small cells,” selectable in the “Grid Generator Advance Options Panel.” In the first case, the cells whose volume is smaller than a user-defined value, set at 4% of the original computational cell, are removed. The main problem related to this possibility is that it tends to create corner, or divots, inside the computational domain, and, in some cases, affecting the particle flow. By choosing instead “merge and remove small cells” option, the position of the cells’ nodes in the region next to boundary wall will be changed in such a way that the corner presence is avoided, but the geometry of the system is distorted and so, instability problems could affect the simulations.

5.2 Simulation set-up

It was chosen to tune the simulation parameters and mesh refining with the configuration characterized by R/D = 6.25 and superficial air velocity equal to 17 [m/s]. The results obtained are then use to the simulate the rest of geometries and operative conditions. The mesh was created leaving the default option “remove volumes” uniformly, increasing the total number of desired cells to refine it. A first trial mesh was created selecting a total number of cells equal to 500000 as showed in Fig. 5.2 a) and b).

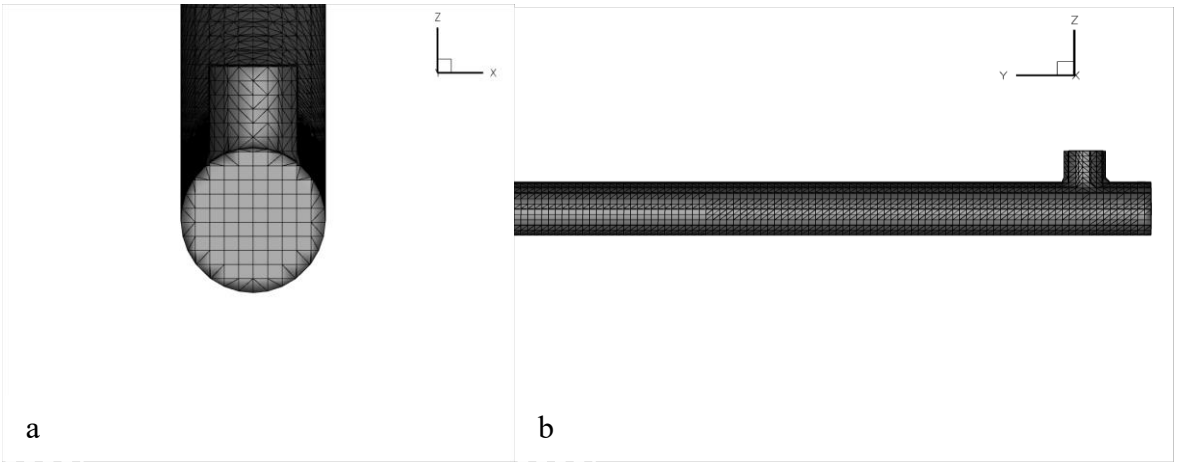

Figure 5.2: (a) mesh of the pipe section, (b) lateral view of the pipe mesh

To make the calculations representative of the simulated system boundary conditions similar to that described in Fei [1] are set. At the outlet section is imposed the pressure to be equal to the atmospheric one, moreover the solid particles are allowed to exit from the pipe once they reach the outlet section. The airflow enters the system from the main pneumatic conveying pipe section with a pressure set at 102000 [Pa] and a Temperature of 300 [K]. The solid enters the system from the solid feed pipe with a solid flowrate fixed to 0.29 [kg/s] with the particle size distribution showed in chapter 3. It must be pointed out that to allow the solid entering the system it is necessary to feed a small airflow along with it, to avoid numerical errors for which the system is not able to recover the desired solid flowrate, moreover it is imposed that the solid is fed with the same velocity of the air. To keep the desired air flux entering the system it is necessary to correct the air velocity at fluid boundary condition by applying the mass conservation principle. The particle feed starts after the first 0.5 [s] of simulation, so, initially from the solid feed section, only air will access the system, to allow the system to go

to regime. After setting the boundary conditions a first try setting for the model parameters was imposed, showed in Tab.5.1, to investigate firstly when the system would have reached a SteadyState condition. The turbulence is described with the large eddy simulation model.

Table 5.1. First trial parameter choice

parameter	Value
θ_{cp}	0.63
M_{max}	0.4
r_N	0.95
r_T	0.95
Diffuse bounce	5
Manual density number	1000
C_D	non-spherical Ganser
ψ	0.77

As depicted in Fig.5.3, the SteadyState is reached after around 3.5 [s], so, it has been chosen to continue the simulations for a total time of 5 [s], in order to perform time averaging on the quantity of interest through the last second of the simulation.

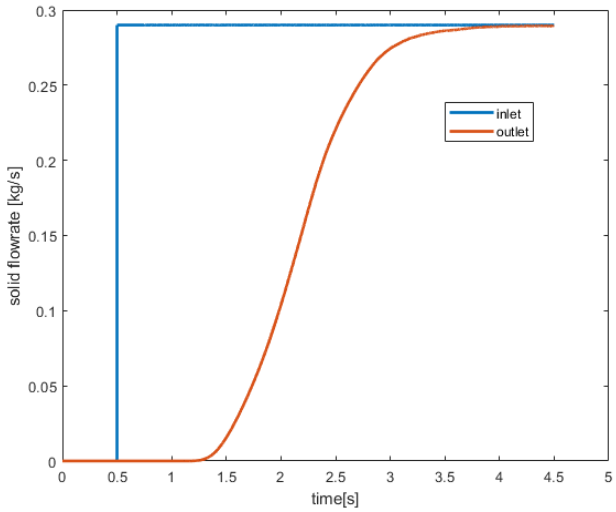

Figure 5.3: Mass balance

5.3 Mesh independence study

To establish when one has to consider that the mesh has no impact on the simulations' results, the total line ΔP are taken as reference parameter, and the impact of mesh refining on it was studied. In Fig. 5.4. the total line ΔP are plotted as function of the total real cells. To find a compromise between the simulations computational cost and the accuracy of the results, it has been chosen to select the mesh with 2e6 total cells, which corresponds to 231360 real cells.

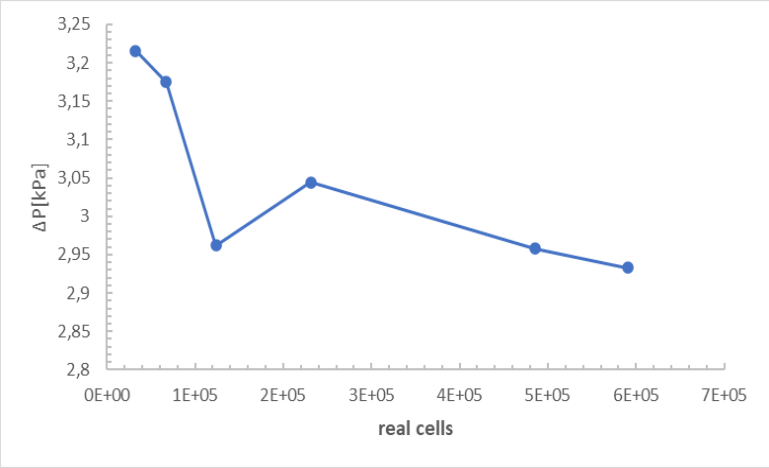

Figure 5.4: Mesh independence study

5.4 Parameters sensitivity analysis

The only particle-particle parameter customizable is the maximum momentum redirection from collision, as the close-pack volume fraction is fixed at 0.63 from the article data and equation (4.11). In Fig. 5.5 the effect of the maximum momentum redirection from collision is depicted. As expected, this parameter has little to null influence, as, operating in dilute phase regime, it is not much probable the presence of zones characterized by particle volume fraction near close-pack limit. For this reason, it has been chosen to leave the default value of 0.4

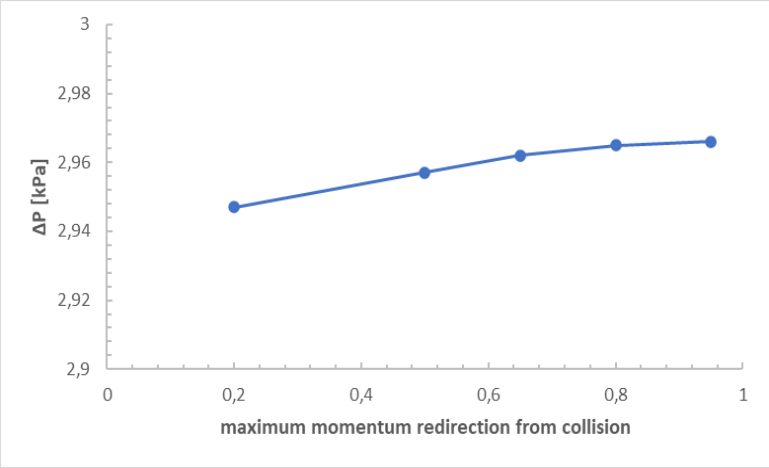

Figure 5.5: Effect of maximum momentum redirection

In Fig.5.6 the effect of the particle to wall interaction parameters is depicted, it should be noted that the tangential component has a stronger influence on the total line ΔP. As the simulated ΔP reported in the article are equal to 2.4 [kPa] both parameters are set to 0.98 to choose the combination that gives the smallest possible ΔP.

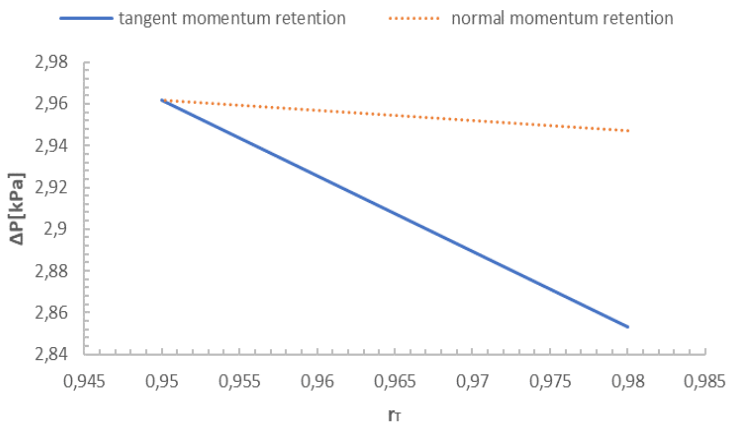

Figure 5.6: Effect of particle-to-wall parameters

One key point is that, if one of these two parameters is set below 0.95, in the proximity of the first bend the particle volume fraction reaches the close-pack limit, the line ΔP grew indefinitely over time and the simulation does not reach the SteadyState condition, as showed in Fig. 5.7

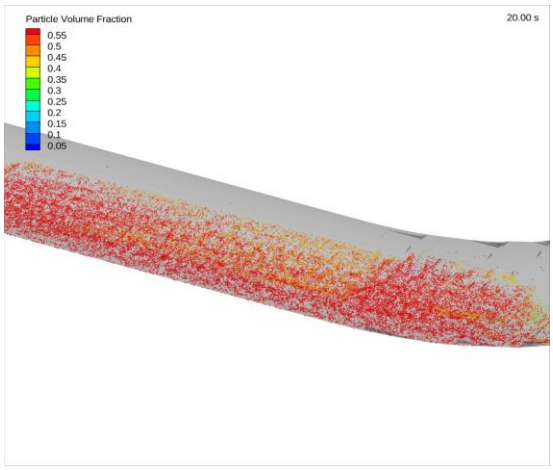

Figure 5.7: Blockage of the pipe

In Fig.5.8 the effect of the diffuse bounce is investigated, showing that it does not have much of an impact, so the default value 5 has been left.

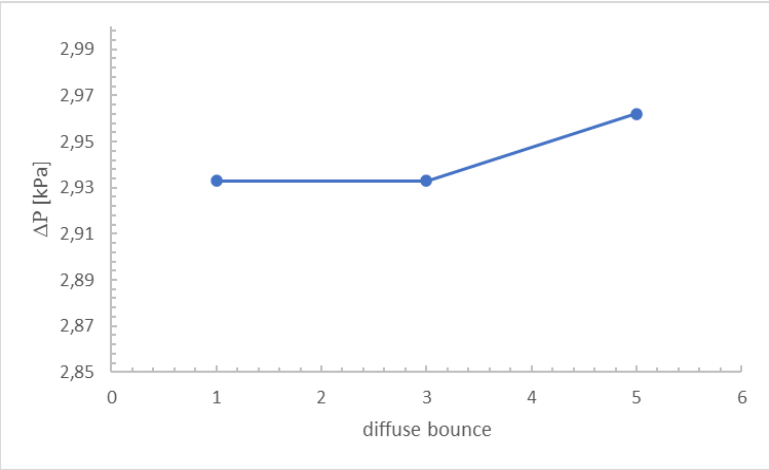

Figure 5.8: Diffuse bounce

Increasing the number density manual makes the calculations statistically more representative of the simulated system: the drawback is that the computational costs increased too, in Fig. 5.9 is showed the trend of line ΔP varying this parameter, it has been chosen to select 1000 for the further simulations.

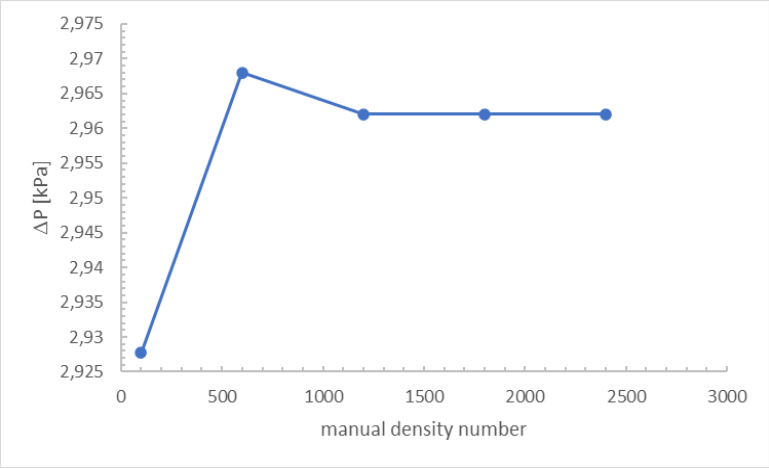

Figure 5.9: manual density number

After the analysis on the effect of each parameter it was found that the most influent parameter on the simulation was the tangent-to-wall momentum retention. In Tab.5.2 are summed up the parameters choice that will be used for the further calculations.

Table 5.2. Parameter choice

parameter	value
θ_{cp}	0.63
M_{max}	0.4
r_N	0.98
r_T	0.98
Diffuse bounce	5
Manual density number	1000
C_D	non-spherical Ganser
ψ	0.77

5.5 Drag Model comparison

After having set the parameters at values showed in Tab.5.2, the impact of the drag models on the macroscopic variables considered in the case study has been studied for R/D =6.25 configuration, varying the superficial air velocity between 15 and 19 [m/s]. The total line pressure drops and the axial and radial component of the particles' velocity at the bend are obtained, to make a comparison with those of the article. The Wen-Yu model is compared to the non-spherical Ganser, previously used to tune the simulation parameters. In Fig. 5.10 the pressure drops obtained with Wen-Yu, and non-spherical Ganser drag models are compared with that of the selected article. With both models a further simulation, at lower superficial air velocity, in comparison with the interval considered in the article, was made to see if the MP-PIC framework is able to predict the dense phase regime

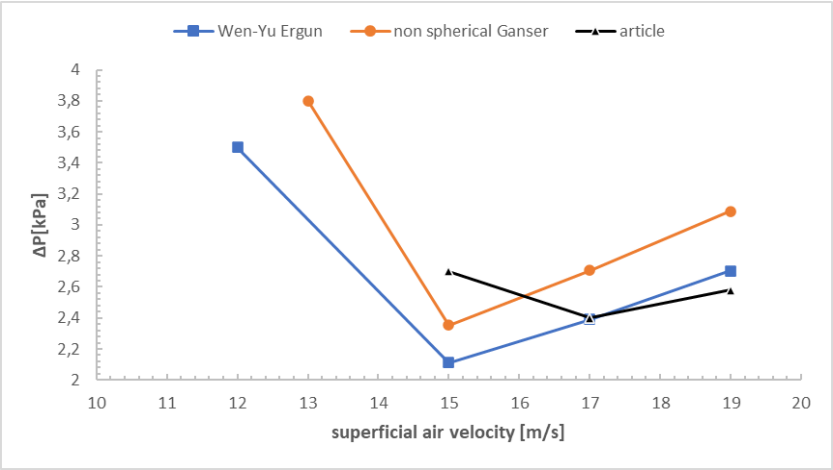

Figure 5.10: phase diagram for R/D = 6.25

In the study interval with both drag models' fair results are obtained in comparison with that of the article, though the local minimum in the line ΔP resulted from the experiments, at a superficial air velocity of 17 [m/s] is not predicted. The particles' axial velocity component at the first bend, averaging through the last second of simulation, for each location of surface

line, as explained in (3.7.2) , is obtained. In Fig. 5.14 this value is normalized with respect to the minimum pressure drops (MDP) air velocity, found in [1] which corresponds to 17 [m/s], defining the averaged axial slip ratio:

$$axial\ slip\ ratio\% = \frac{\mathbf{u}_{p,axial}}{\mathbf{u}_{air,MPD}} \times 100\% \tag{5.1}$$

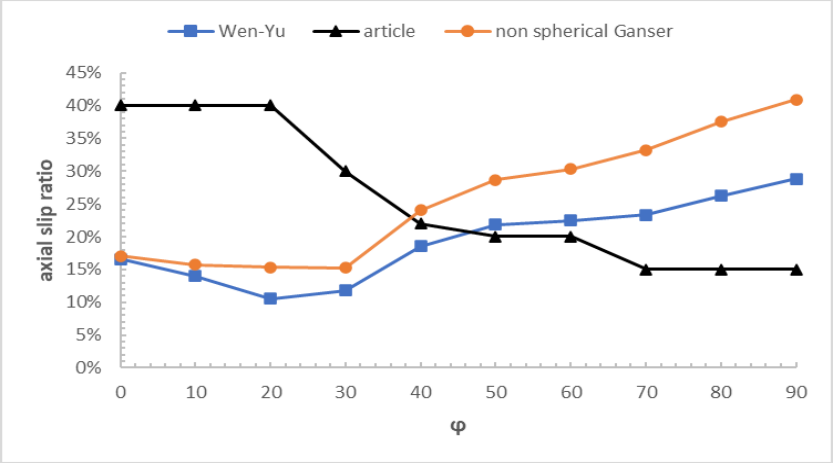

Figure 5.11: averaged axial particle slip ratio

The CFD code cannot predict properly the trend of particles averaged axial velocity, as the particles accelerate through their motion through the bend. The resulting error is high, especially in the region $0 \leq \varphi \leq 40°$. The same procedure is followed for the particles' averaged radial velocity component, in Fig. 5.12 is showed averaged radial slip ratio, obtained normalizing with respect to the minimum pressure drops air velocity the averaged radial velocity component:

$$radial\ slip\ ratio\% = \frac{\mathbf{u}_{p,radial}}{\mathbf{u}_{air,MPD}} \times 100\% \tag{5.2}$$

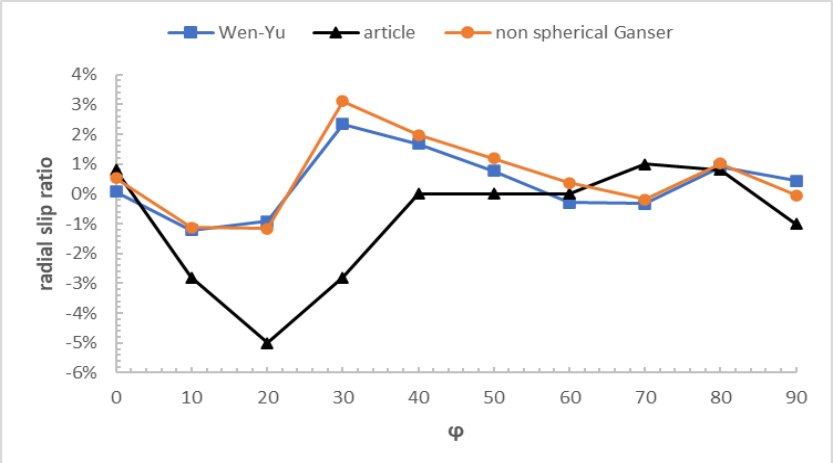

Figure 5.12: averaged radial particle slip ratio

In this case the MP-PIC model initially predicts the right trend, underestimating in the very first trait the particles' velocity, performing well from φ≥ 40° on. As overall the Wen-Yu drag model performs better, especially regarding the averaged particles' axial velocity, it would be employed to analyze the configurations with R/D = 5 and R/D = 3.75.

5.6 R/D effect

The same procedure, choosing Wen-Yu drag model, as written above, is followed for the remaining geometrical configurations with respectively R/D = 5 and R/D = 3.75. In fig. 5.13 and 5.14 the pipeline pressure drops are showed respectively for R/D = 5 and R/D=3.75. The MP-PIC method predicts that, at fixed superficial air velocity, the pressure drops would diminish decreasing R/D, while the experimental showed exactly the opposite behavior. It has to be said though that the magnitude of the pressure drops changing varying R/D is not high both in the simulations' results and in the article. In general, the results are quite accurate, as the relative error does not rise above 20%.

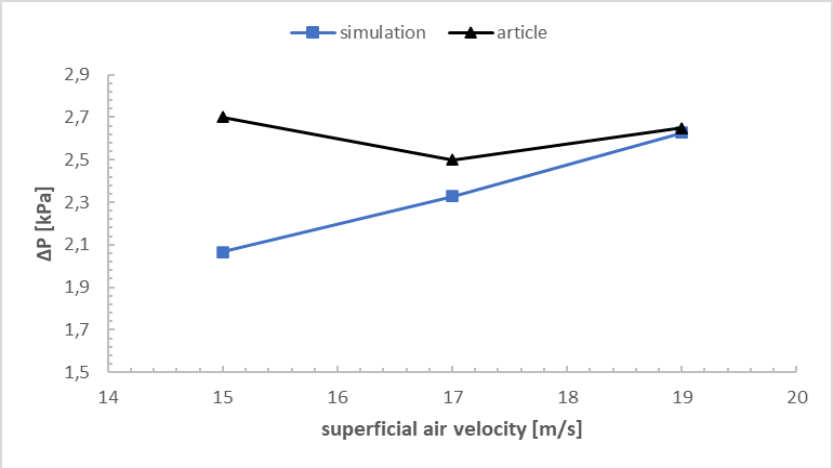

Figure 5.13: Phase diagram for R/D = 5

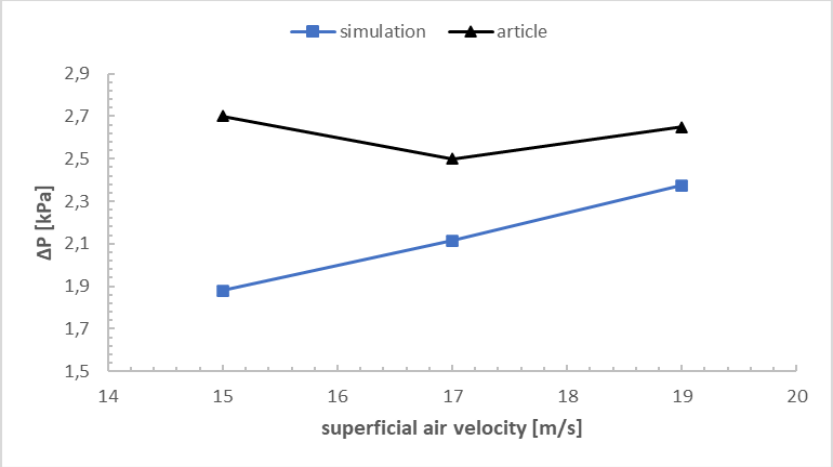

Figure 5.14: Phase diagram for R/D =3.75

In fig. 5.15 and 5.16 the averaged particles' axial slip ratio is shown respectively for R/D = 5 and R/D=3.75. As for R=6.25 the MP-PIC method is not able to predict the right trend, and, especially at the bend inlet, the relative error with respect to the article is high. Moreover, contrary to the experimental results, decreasing R/D the inlet bend averaged superficial slip ratio increases.

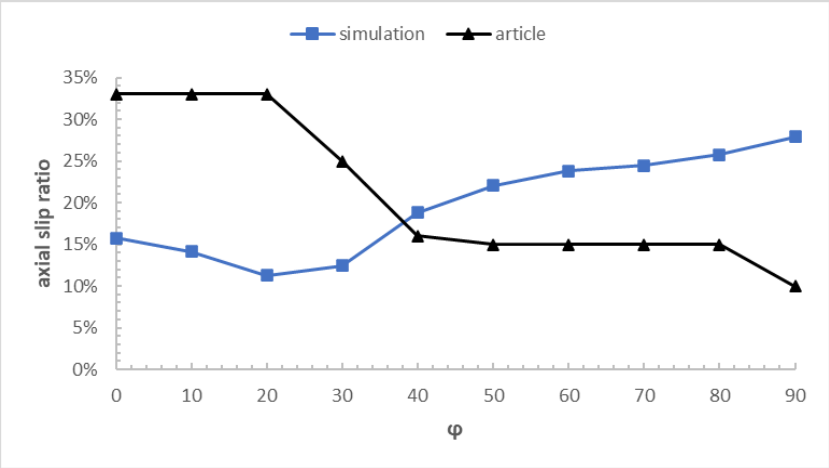

Figure 5.15: Averaged particles' axial slip velocity for R/D =5

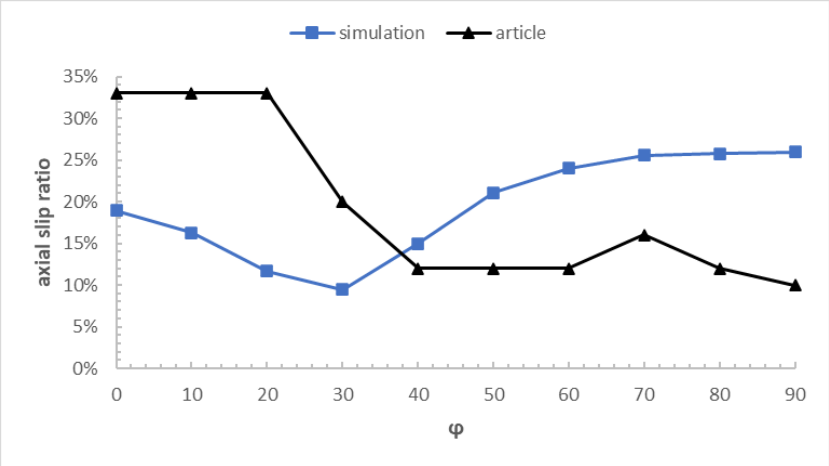

Figure 5.16: Averaged particles' axial slip velocity for R/D =3.75

In Fig. 5.17 and 5.18 the averaged particles' radial slip ratio is shown respectively for R/D = 5 and R/D=3.75. The trend of the experimental results is well predicted, but, as-before, the MP-PIC method underestimates the centrifugal acceleration that pushes the particles against the outer pipe wall, as the particles' averaged radial slip ratio for $\varphi \geq 40°$ is underestimated. On the other side, as showed in Fig. 5.17, the increasing in averaged particles' slip ratio with decreasing of R/D is well predicted.

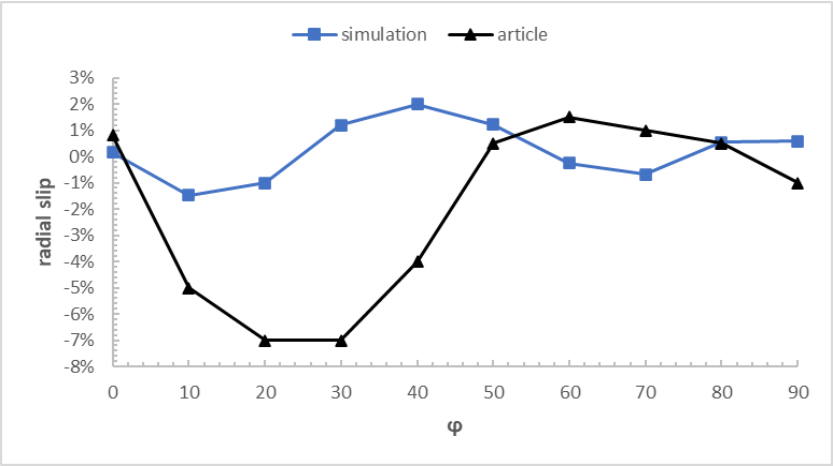

Figure 5.17: Averaged particles' radial slip velocity for R/D =5

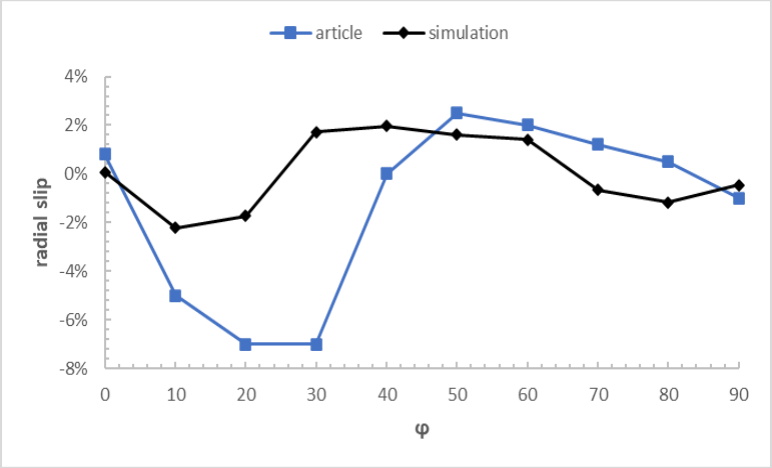

Figure 5.18: Averaged particles' radial slip velocity for R/D =3.75

In Fig. 5.19 the simulated pressure drops at the first bend are compared with the results obtained from the correlation reported in Section 3.5. The values predicted by the model are in fair agreement with those of the correlation, as low errors are present.

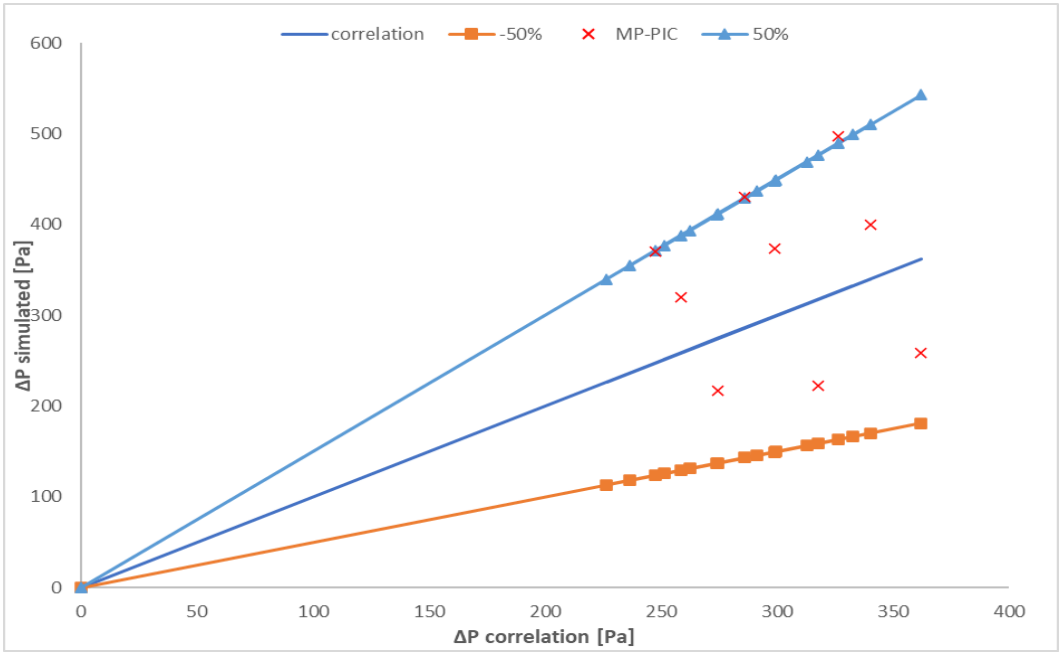

Figure 5.19: Simulated vs correlation ΔP at the first bend

6. Two Fluid Model

The two fluid model (TFM) was set-up in Ansys Fluent version 2021 R2.

6.1 Mesh generation process

To obtain reliable results, applying Euler-Euler TFM, the mesh must be constituted by hexahedral cells, as the tetrahedral one can led to less accurate results. Because of the difference in diameter between the solid entrance duct and the main conveying pipe, it was impossible to obtain a fully hexahedral mesh, so the geometry was splitted into two regions: the first one comprehends the first 20 [cm] of the main duct and the solid entrance, while the second one the rest of the pipe.

To create these two regions, the geometry file was imported in Design Modeler, where a new plane was defined selecting the option "define from point and normal." After that, a slice was created to subdivide the solid into two regions using the "define new slice" option. To mesh the solid is necessary to make sure that the nodes of the two parts are connected: if this does not happen numerical problems during the calculation can occur and so the results will not be dependable. To merge the nodes firstly it is necessary to create a new part, formed by the two regions previously created, and then to apply the "share topology option."

The mesh was created with the "Fluent Meshing" tool; firstly, it was decided to insert inflation into both parts: as the pneumatic conveying line works in a dilute phase regime the particle-wall interactions are particularly important, so have a more refined mesh in correspondence of the wall can help to capture the key features of the flow. Then, as the feeding solid pipe diameter is half the size of the main pipe a "sizing" was inserted, and it was decided to select as "element size" half the dimension of the main pneumatic conveying line. Finally, a Multizone method is applied to the geometry region that follows the first 20 [cm] to obtain hexahedral cells while the first part is constituted by an unstructured mesh as showed in Fig.6.1 .

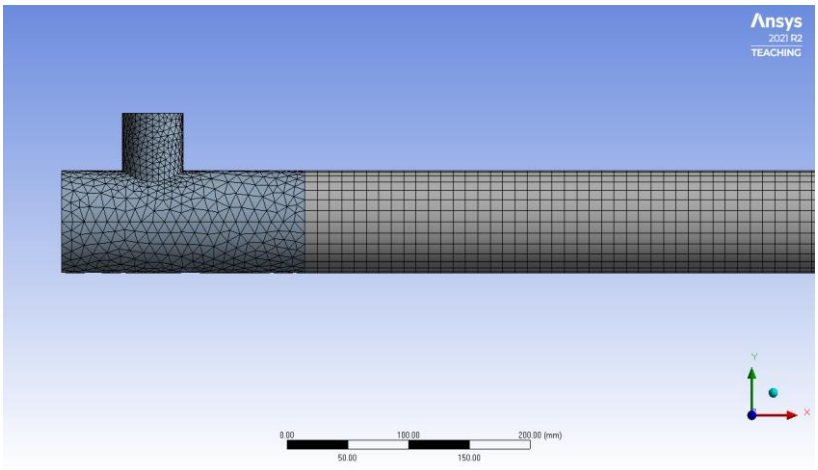

Figure 6.1: Mesh output

As previously said, the "share topology option" selected in Design modelling assures that the nodes at the interface between these two regions are merged, as showed in Fig.6.2

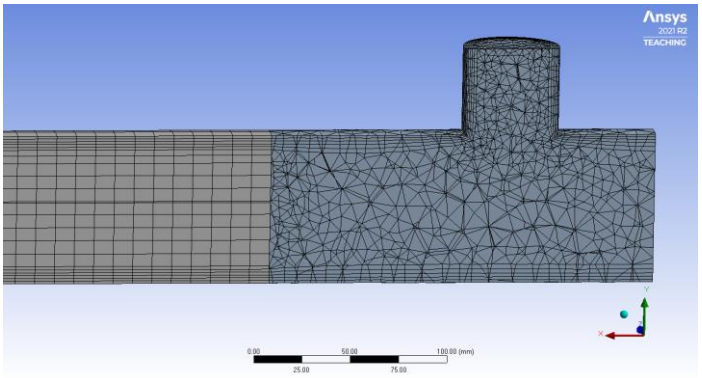

Figure 6.2: Nodes merging at mesh interface

6.2 Simulation set-up

Boundary conditions representative of those ones described in Fei [1] are set. At the outlet section is imposed the pressure to be equal to the atmospheric one, as the solid particles in this framework are seen as a fluid, in this case it was not necessary to impose the particles to exit from the pipe once they reach the outlet section.

The airflow enters the system from the main pneumatic conveying pipe section with a pressure set at 102000 [Pa] and a Temperature of 300 [K]. The solid enters the system from the solid feed pipe with a solid flowrate fixed to 0.29 [kg/s]. As in the Two Fluid Model framework including the particle size distribution requires a lot of memory and additional computational time, it has been chosen to set the particle diameter at 4.22 [mm], defined in Fei et al. [1] as the equivalent particle diameter.

Along with the solid a small airflow is fed, and a unitary slip ratio between these two is imposed, to avoid numerical problems, to maintain the flux of air at the desired value a correction in the feeding air section is done applying the principle of conservation of mass. In this framework, the solid phase enters the system at the same time of the fluid one. After setting the boundary conditions a first try setting for the model parameters was imposed, indicated in Tab.6.1, obtained from [32] to investigate firstly when the system would have reached a SteadyState condition. As reported in Section (3.7) the following considerations are referred to the configuration characterized by R/D and superficial air velocity respectively of 6.25 and 17 [m/s]. The turbulence is described with the *dispersed k-ε* model along with a *standard wall function.*

Table 6.1. First trial parameter choice

parameter	**Model**
$\mu_{s,kin}$	10^{-5}
λ_s	null
Θ_s	algebraic
p_s	Lun et al.
$g_{0,ss}$	Lun et al.
Elasticity Modulus	derived
Packing limit	0.63

Drag model	Wen-Yu
e_{ss}	0.9
φ	1

The solution methods, showed in Tab. 2, are set with the suggested values from Ansys Guide[32]:

Table 6.2. Solution methods: Pressure-velocity coupling

parameter	Model
Scheme	10^{-5}
Gradient	Least Squares Cell Based
Pressure	PRESTO!
Momentum	First Order Upwind
Volume fraction	First Order Upwind
Transient formulation	First Order Upwind

As showed in Fig. 6.3 the SteadyState is reached at approximately 3.5 [s], so the simulations are executed for 5 [s] to calculate average quantities through the last second of simulation.

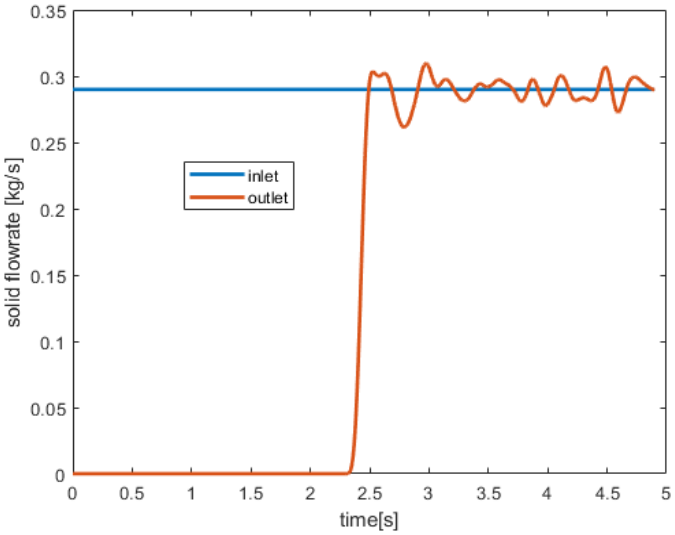

Figure 6.3: Mass Balance

6.3 Mesh independence Study

In general, the quality of the mesh plays a key role to guarantee the accuracy and stability of the simulation that will be performed; so, to check the quality of the meshes that will be assessed, it has been chosen to look for orthogonal quality, skewness, and aspect ratio. The orthogonal quality of a cell is defined as the minimum value, computed for each i-face of a given i-cell, from:

$$\begin{cases} \dfrac{\mathbf{A}_i \cdot \mathbf{f}_i}{|\mathbf{A}_i||\mathbf{f}_i|} \\ \dfrac{\mathbf{A}_i \cdot \mathbf{c}_i}{|\mathbf{A}_i||\mathbf{c}_i|} \end{cases} \tag{6.1}$$

Where $\boldsymbol{A_i}$ is the area vector of a face, $\boldsymbol{f_i}$ is the vector formed from the centroid of the i-cell to the centroid of the face, and $\boldsymbol{c_i}$ is the vector that links the centroid of the i-cell to the centroid of the adjacent cell sharing a face with the i-cell consider, as showed in fig. 6.4

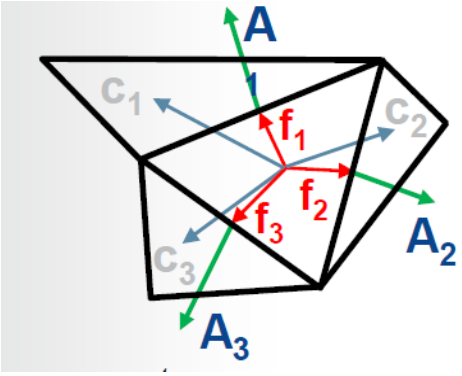

Figure 6.4: vectors employed to describe the orthogonal quality

The orthogonal quality of each cell ranges from 0 to 1, the closest to 1 this value is, the highest quality of the cell. In general, the minimum acceptable value for this parameter is 0.01.

Another important parameter is the aspect ratio, which measures the stretching of a cell, it is computed as the ratio between the maximum distance from the center of the cell to a node and the minimum distance between the center of the cell and the center of a face. Typically, it is better not to work with a high value of this parameter, especially if the flow shows strong gradients in the direction where the aspect ratio is bigger.

Finally, Skewness is the difference between the shape of the cell and the shape of an equilateral cell with equivalent volume. For a mesh constituted by triangular/ hexahedral elements, the maximum skewness should be below 0.9, with a significantly lower average value. If this condition is not respected there will be convergency problems in the simulation. In Tab. 6.3 the key features of the tested mesh, generated as described in Section 6.1 are shown

Table 6.3. evaluated mesh characteristics

Parameter	Mesh 1	Mesh 2	Mesh 3	Mesh 4	Mesh 5
Number of elements	125927	237912	346595	694601	1036970
Minimum orthogonal quality	0.1	0.12	0.11	0.18	0.15
Average orthogonal quality	0.96	0.97	0.97	0.97	0.97
Maximum skewness	0.9	0.88	0.89	0.82	0.84
Average skewness	0.16	0.13	0.14	0.13	0.12
Maximum aspect ratio	12	13	13	13.9	12.5
Average aspect ratio	5.6	5.1	4.7	4.3	4

As previously described (see Section 5.2) the pneumatic conveying line ΔP, obtained by averaging through the last second of simulation, are taken as reference parameter to do the analysis. From Fig. 6.4 it is possible to see a good compromise between the mesh refining impact and the computational cost on the selected parameter is reached when mesh 2 is adopted.

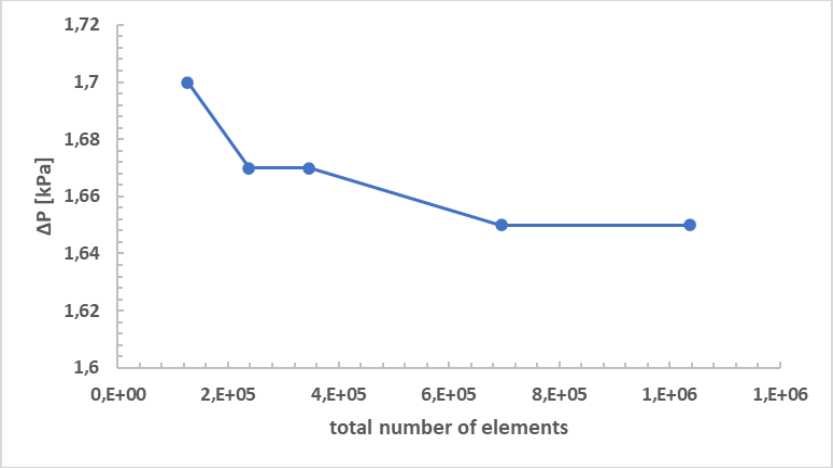

Figure 6.4: Mesh independence study

6.4 Sensitivity analysis parameter

The impact on the model of the lift force, turbulent interaction, and turbulent dispersion force, has been studied by making a comparison with the case in which neither of these terms was included. From Fig. 6.5 these additional sources have a limited impact, so, as they only introduce additional computational costs, it has been decided to not include them for further analysis.

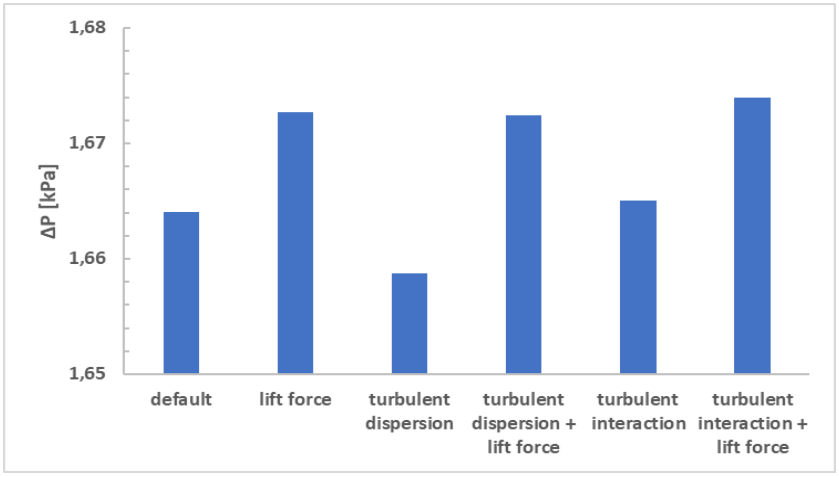

Figure 6.5: Effect of additional terms

In Fig. 6.6 a sensitivity analysis on the coefficient of restitution is showed, this parameter has not much of an impact on the reference parameter, so the default value of 0.9 is kept.

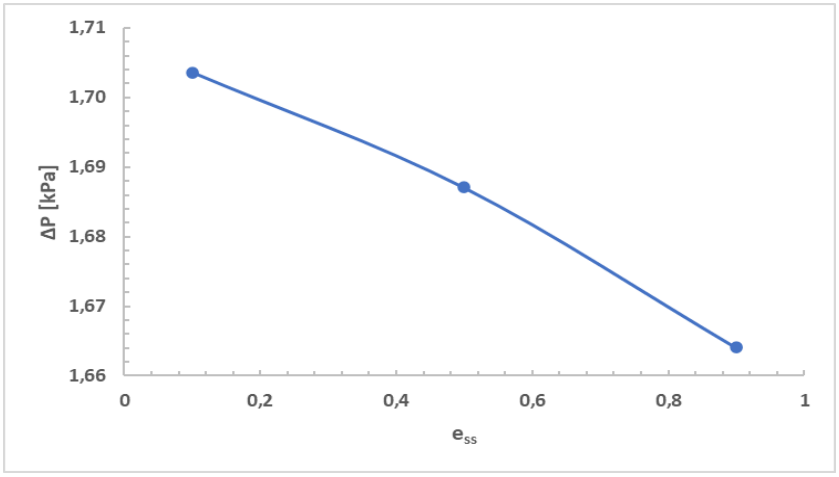

Figure 6.6: Sensitivity analysis on the coefficient of restitution

As the previewed pneumatic conveying line are so far considerably lower in comparison to that of the article, the Syamlal O'Brien model is introduced to describe the kinetical part of the solid shear viscosity, originally set at a constant value of 10^{-5} as reported in Tab. 6.2. This leads to an increase of the pneumatic conveying line ΔP, so the specularity coefficient, initially set at 1, is tuned, as showed in Fig. 6.7, to obtain a ΔP value close to that of the article .

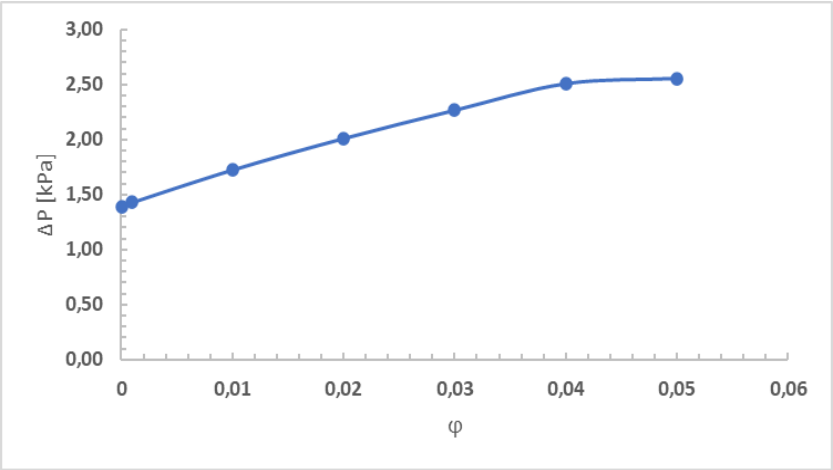

Figure 6.7: Sensitivity analysis on the specularity coefficient

By comparison with the experimental results, it appears that choosing φ=0.03 is the best fit.

The granular bulk viscosity initially set at zero, as reported in Tab. 6.1 is now described with the Lun et al. model [23], to see how this affects the reference parameter. As shown in Fig.6.8 the impact is negligible, so, to minimize the computational cost, it is set to zero.

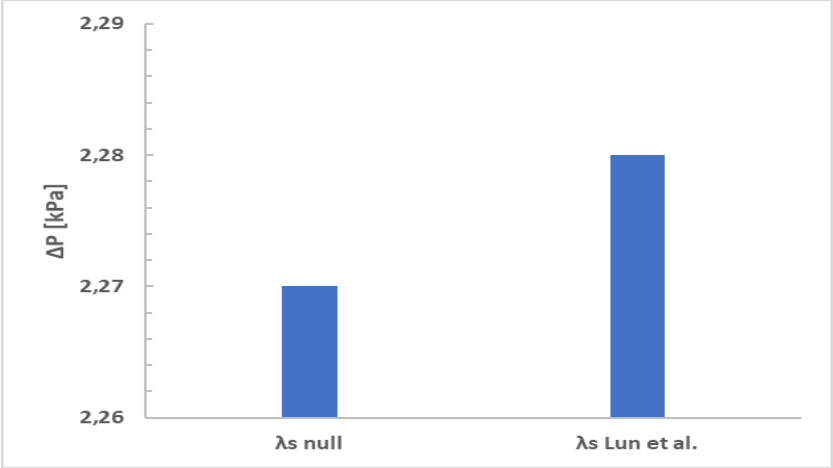

Figure 6.8: Granular bulk viscosity impact

After this analysis, the parameter selection to further simulations is reported in Tab. 6.4

Table 6.4. Final parameters selection

parameter	Model
$\mu_{s,kin}$	Syamlal O'Brien
λ_s	null
Θ_s	algebraic
p_s	Lun et al.
$g_{0,ss}$	Lun et al.
Elasticity Modulus	derived

Packing limit	0.63
e_{ss}	0.9
φ	0.03

6.5 Drag models

After having set the parameters at values showed in Tab.6.2, the impact of the drag models, is studied for the configuration characterized by R/D equals to 6.25. The superficial air velocity is varied between 15 and 19 [m/s] and the total line pressure drops along with the axial and radial component of the particles' velocity at the bend are obtained.

The Wen-Yu model is compared to the Syamlal O'Brien drag model; it is important to remark that this drag model can be employed only when the kinetical part of the solid shear viscosity is modeled with the Syamlal O'Brien model, as it is the case. In Fig. 6.9 the total line pressure drops are depicted, showing that the two models give close predictions.

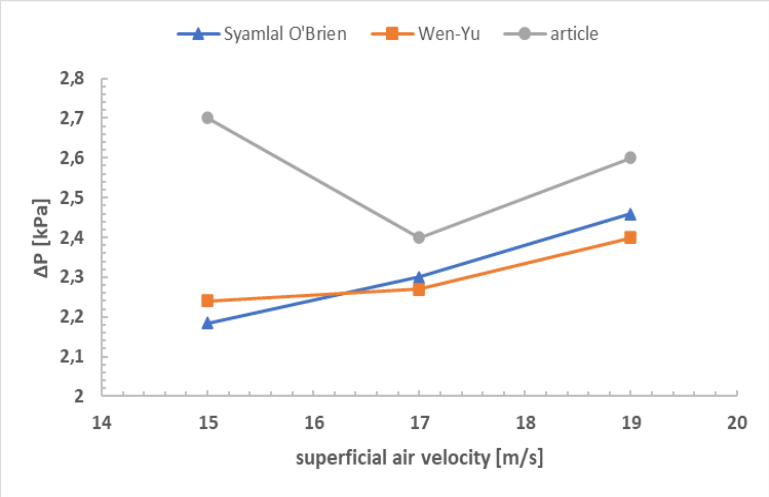

Figure 7.9: Drag models comparison: total line pressure drops

In Fig. 6.10 and 6.11 the averaged particles' axial and radial slip ratio, defined in Section (5.7), at the first bend are obtained as function of the angle φ are shown.

In general, the predictions of the two models are pretty close for all the macroscopical variables compared, however, as the results on the axial slip ratio are slightly better with the Syamlal O'Brien drag model, this will be employed to investigate the effect of varying the bend radius on the macroscopical variables selected. In general, as can be seen, the results are in fair agreement with the simulations, with the main inconsistencies that concerns the averaged particle radial slip ratio, especially for $\varphi<30°$.

This is due to an underestimation of the centrifugal acceleration that the particles experienced when entering the bend, which makes the particles collide against the inner wall of the pipeline. Another issue regards the average particle axial slip ratio: the model underestimates the velocity at which the particles enter the bend.

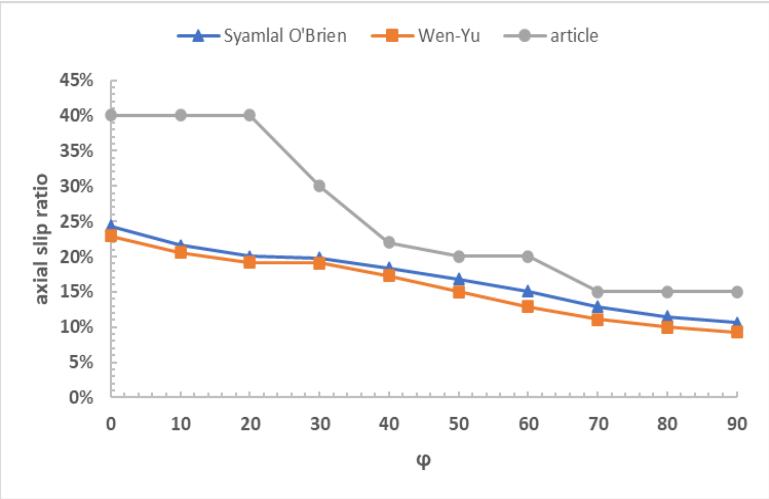

Figure 6.9: Drag models comparison: averaged particle axial slip ratio

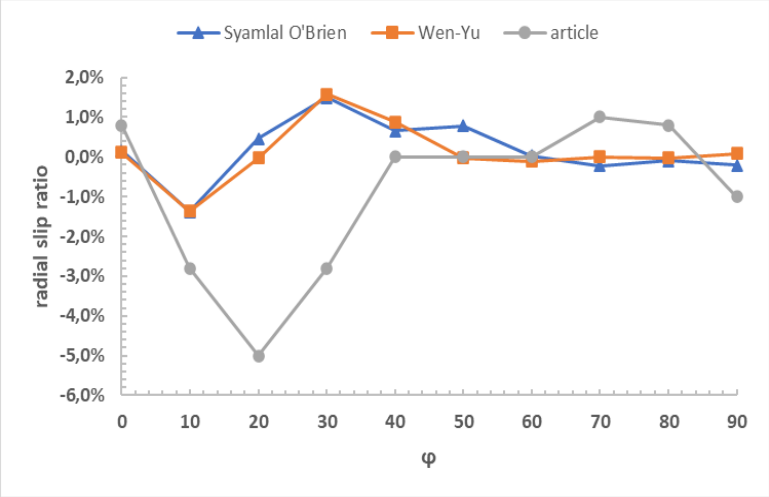

Figure 6.10: Drag models comparison: averaged particle radial slip ratio

6.6 R/D effect

The macroscopical variables of interest, as done in Section 5.9 are obtained for every configuration of bend radius and compared with the experimental results of the article. As showed in Fig. 6.11 and 6.12 the previewed ΔP are in fair agreement with the results. As for the MP-PIC method the software is not able to predict, at equal conditions, an increase of the ΔP with the decreasing of the bend radius. In particular, the bend radius variation does not seem to have an impact on the ΔP.

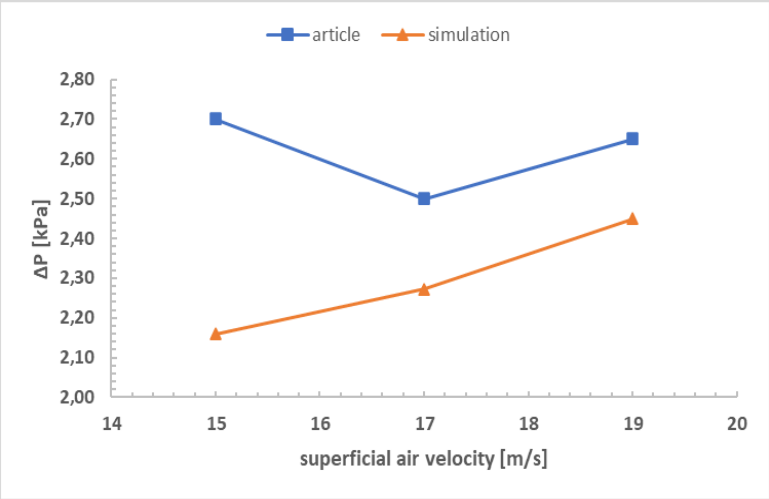

Figure 6.11: Phase diagram for R/D = 5

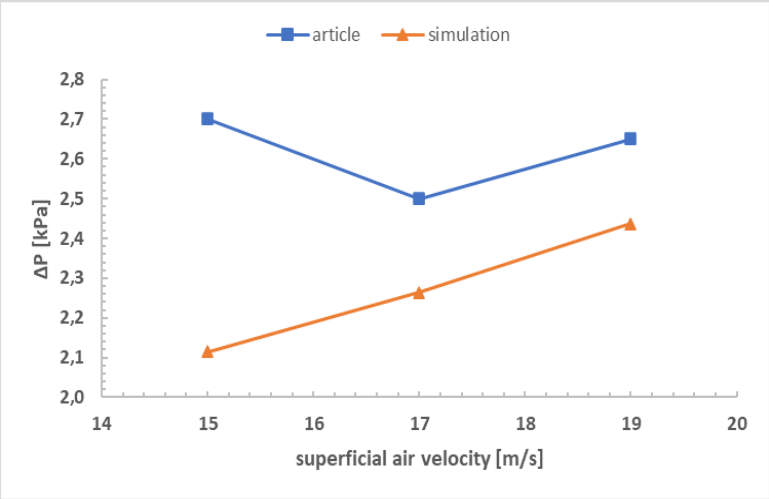

Figure 6.12: Phase diagram for R/D = 3.75

As showed in Fig. 6.13 and 6.14, the model well predicts the trend of particle average axial slip ratio but underestimates again the axial velocity at which the particles enter the bend, the model predictions moreover, seem independent from the bend radius.

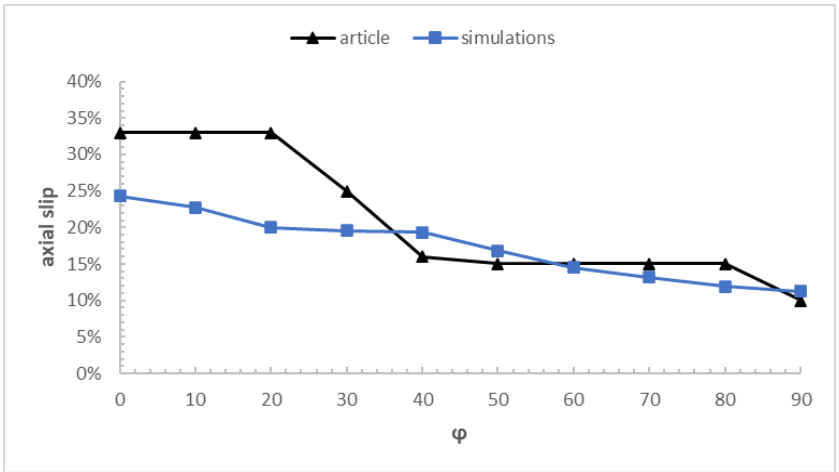

Figure 6.13: averaged particle axial slip ratio for R/D = 5

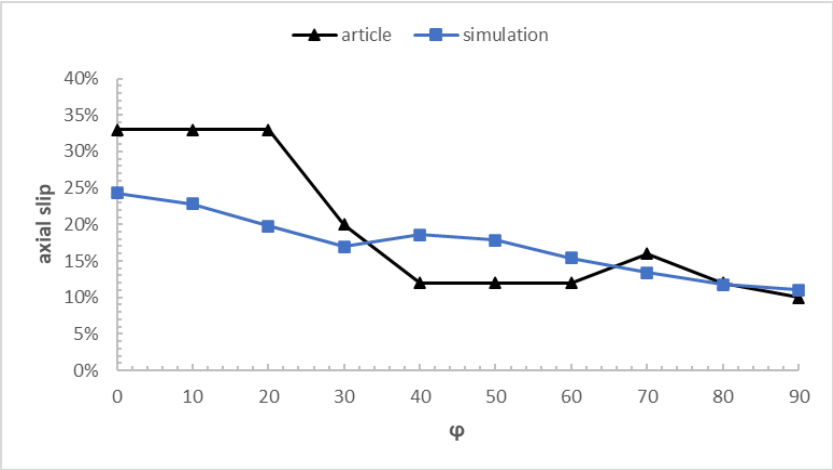

Figure 6.14: averaged particle axial slip ratio for R/D =3.75

In Fig. 6.15 and 6.16 the averaged particle radial slip ratio for, respectively, R/D =5 and R/D=3.75 is shown, even in this case the centrifugal acceleration which the particles experience when they enter the bend is not well predicted, as the radial velocity component that pushes the particles against the inner wall pipe is underestimate. Moreover, the particles start to reaccelerate before in comparison of what obtained from the experimental results.

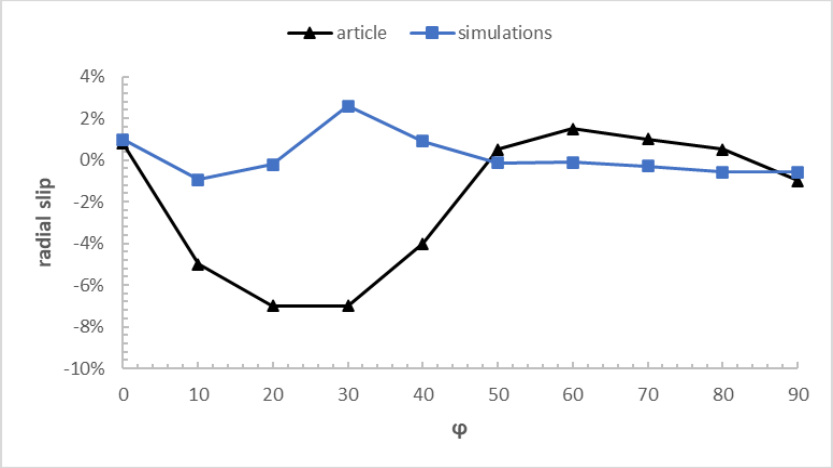

Figure 6.15: averaged particle radial slip ratio for R/D =5

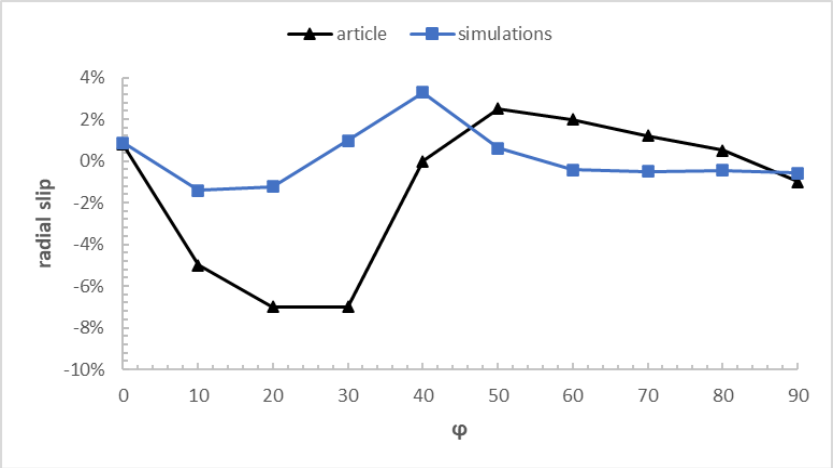

Figure 6.16: averaged particle radial slip ratio for R/D =3.75

In Fig. 6.17 the simulated pressure drops at the first bend are compared to that obtained from the correlation reported in Section 3.5. The TFM predictions are not in fair agreement with the values provided by the correlation, even though large errors are not present.

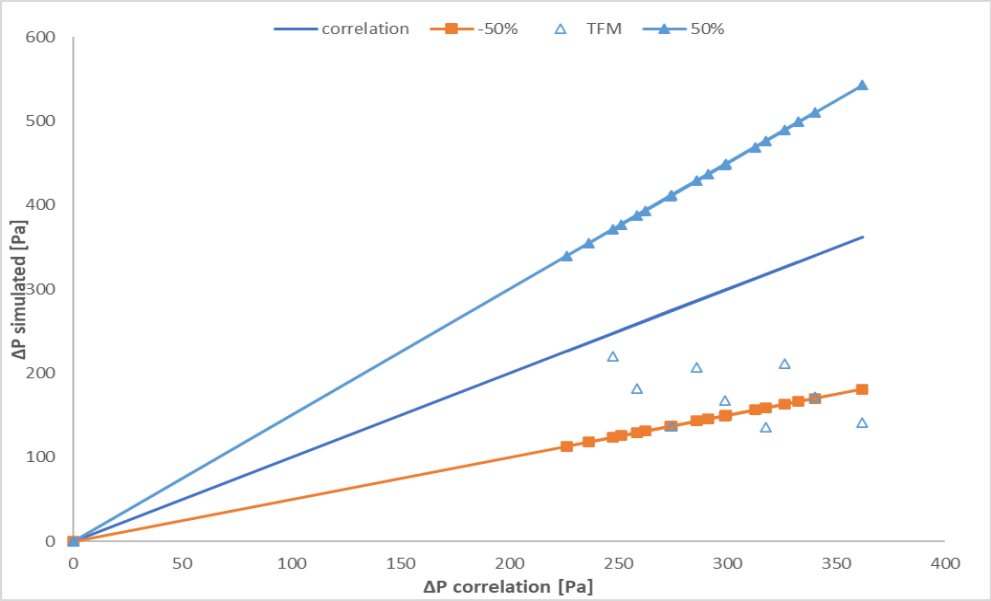

Figure 6.17: Simulated vs correlation ΔP at the first bend

7. Discrete phase method two-way coupling

The Discrete Phase Model has been simulated with the software Ansys Fluent version 2021R2.

7.1 Simulation set-up

To execute the simulations the same mesh described in Section 7.1 has been used. In particular the simulations are performed with mesh 2, which main characteristics are depicted in Tab. 7.3. This is done because in the DPM two-way coupling framework the volume of a particle must be smaller with respect to the volume of a cell, and so there is a limitation on the mesh refining. The particles' size is characterized with the Rosin-Rammler diameter distribution method:

$$Y = 1 - \exp\left[-\left(\frac{d}{\phi}\right)^{n}\right] \tag{7.1}$$

Where d is the particle diameter, which is the independent variable, Y is the particle mass fraction of particles of diameter smaller than d, ϕ is the size constant, defined as the value of d such as Y equals to e^{-1}, and n is the size distribution parameter. In Fig. 8.1 is showed the cumulative distribution function of the study case, obtained from Fei et al.[1].

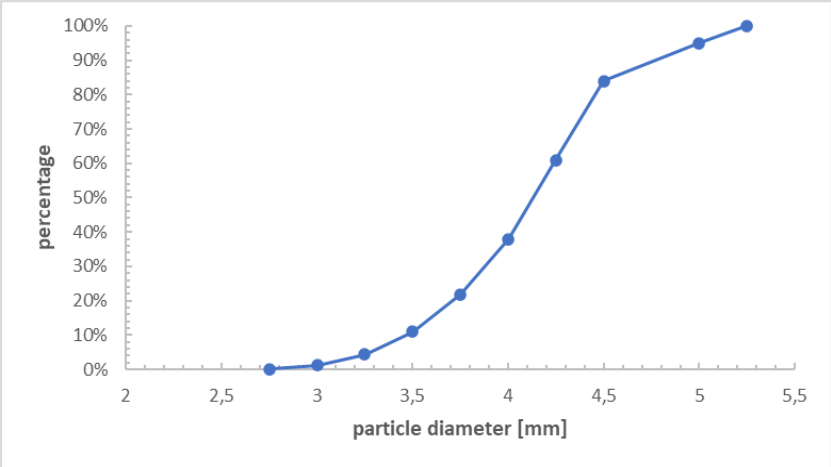

Figure 8.1: particles' diameter cumulative distribution function

From the cumulative distribution function, it is derived that ϕ is equal to 4.399 [mm]. To obtain n at each couple d and Y is applied the equation:

$$n = \frac{\ln\left(-\ln\left(1-Y\right)\right)}{\ln\left(d/\phi\right)} \tag{7.2}$$

To determine which is the value of n that fits the most the particles' diameter cumulative distribution depicted in the article, from all the n is seek the one for which the infinity norm of the difference between the article and Rosin-Rammler method particles cumulative distribution function, defined as:

$$\left\| Y_{article} - Y_{simulation} \right\|_{\infty} = \max_{1 \le i \le n} \left| \left(Y_{article,i} - Y_{simulation,i} \right) \right| \tag{7.3}$$

It is found that n equals to 11.53 gives fair agreement, as showed in Fig. 7.2

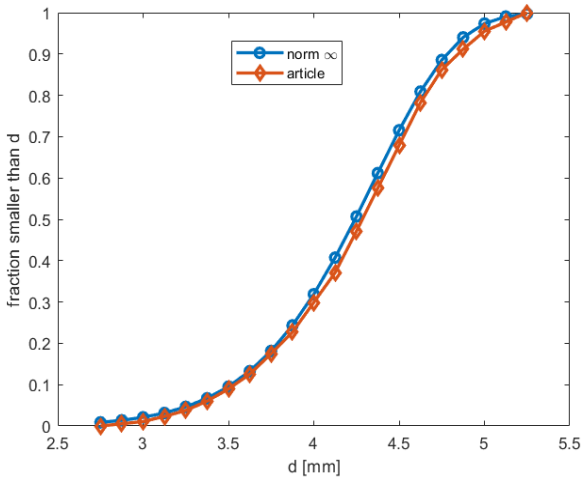

Figure 7.2: comparison between article and Rosin-Rammler particle cumulative distribution function

7.2 Boundary conditions

At the outlet section is imposed the pressure to be equal to the atmospheric one. For the particles, the escape option is imposed, so that they are allowed to exit from the pipe once they reach the outlet section. The interaction between the dispersed and the continuous phase is imposed, so that the two phases affect each other.

The airflow enters the system from the main pneumatic conveying pipe section with a pressure set at 102000 [Pa] and a Temperature of 300 [K]. The particles enter the system at the fluid flow timestep, through surface injection, defined in correspondence of the solid feed pipe section, and the solid flowrate is set at 0.29[kg/s]. The maximum number of timestep to track the particle is set at the same value of the simulation time, so that no particle is lost before it actually exits the system. Moreover, the reflection option is activated so that the particles, once they collide against the wall, will be redirected. Even in this case a small airflow is fed along the solid, to avoid numerical errors. To keep the desired air flux entering the system it is necessary to correct the air velocity at fluid boundary condition by applying the mass conservation principle. The particle feed starts after the first 0.5 [s] of simulation, so, initially from the solid feed section, only air will access the system, to allow the system to go to regime. To calculate the drag coefficient the non-spherical Haider Levenspiel model is chosen, and, for the first trail simulation, the normal and tangent reflection coefficient are set equals to 1.

For the solver option the set-up showed in Tab. 7.2 is adopted. In Fig. 7.3 it is showed that, with the boundary conditions described above, the Steady State is reached close to 1.5 [s], further simulations are then conducted for 3 [s] to obtain averaged quantities through the last second of simulation. To describe the turbulence the *standard k-ε* model is adopted, along with a standard wall function.

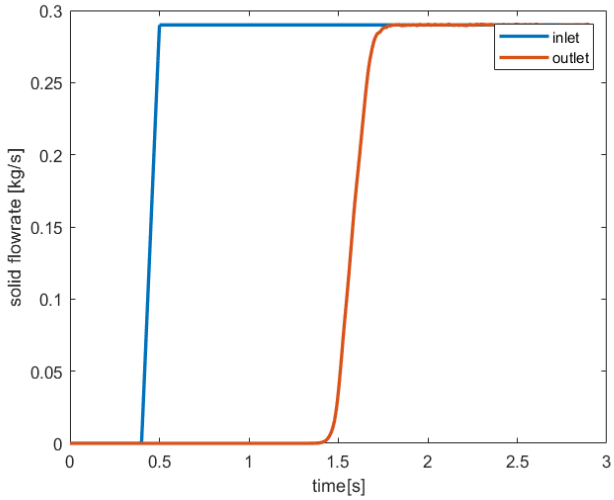

Figure 7.3: Mass balance

7.3 Reflection coefficient

Normal and tangent reflection coefficient are kept both at the same value and varied to tune the simulation ΔP with that of the article; by comparing the simulated and experimental value, as showed in Fig. 8.4, it emerges that fair agreement are obtained setting both coefficients at 0.93.

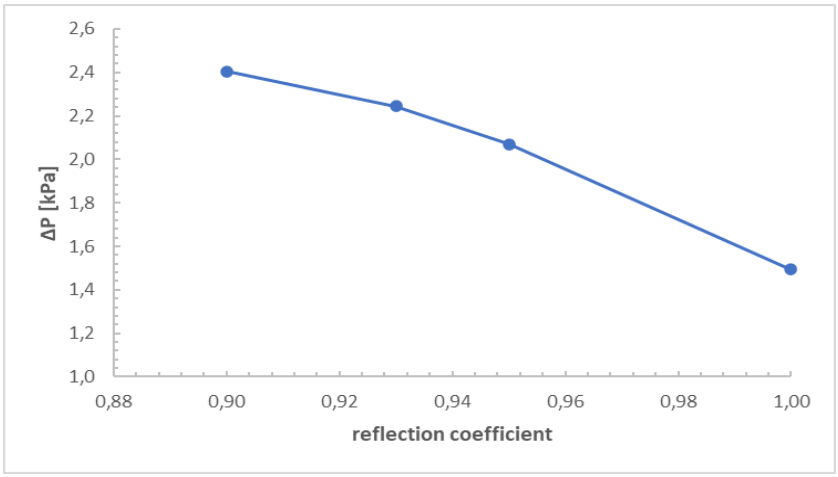

Figure 7.4: Sensitivity analysis on the reflection coefficient

7.4 R/D effect

In Fig. 7.5, 7.6 and 7.7 the total pneumatic conveying line pressure drops are depicted as function of the superficial air velocity. As for the other frameworks the predictions are in fair agreement with the experimental results, on the other side, this is the only model that predicts at equal superficial air velocity, increasing in ΔP when R/D is decreased, this is coherent with the experimental data.

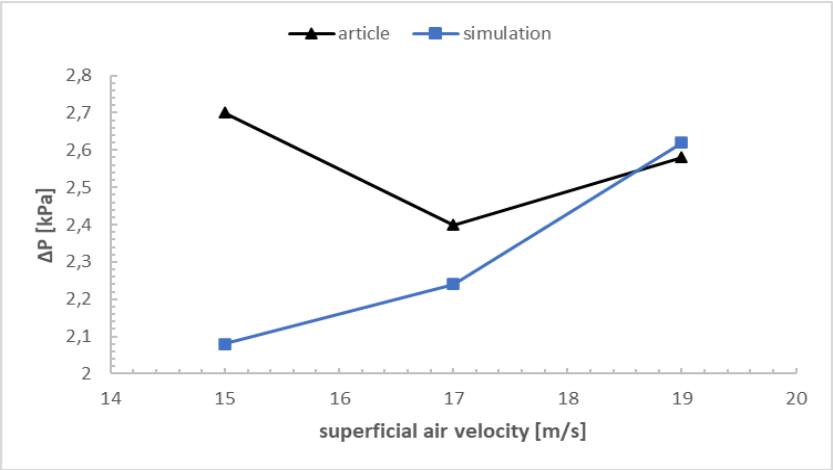

Figure 7.5: Phase diagram for R/D = 6.25

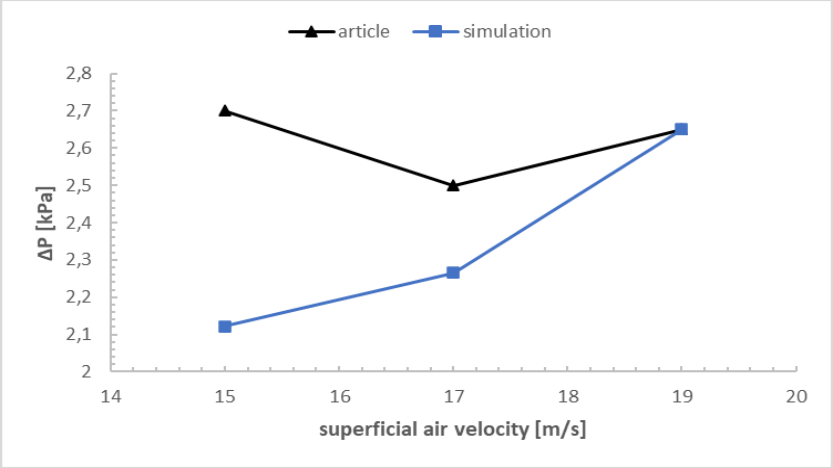

Figure 7.6: Phase diagram for R/D = 5

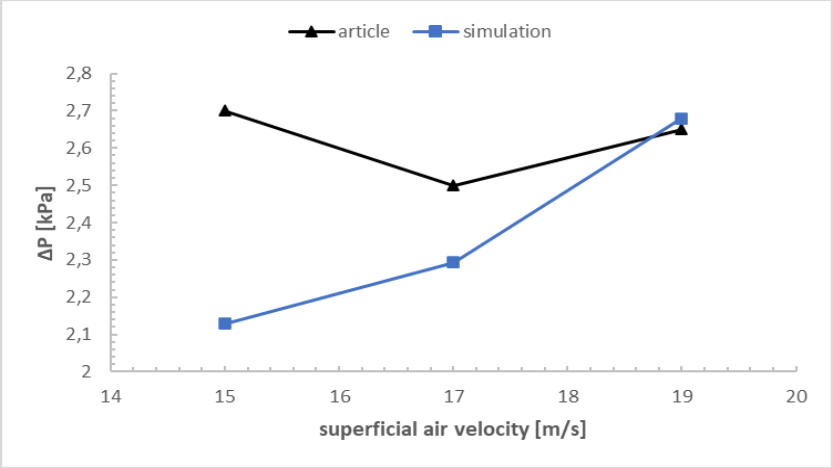

Figure 7.7: Phase diagram for R/D = 3.75

The predicted averaged particles' axial slip ratio is in fair agreement with the experiments, in particular this is the only framework that does not underestimate the particles' inlet velocity at the bend, even if the particles start to decelerate before. As showed in Fig. 7.8, 7.9 and 7.10, the variation in R/D has not a significant impact on the simulations, in the experiments instead

it is showed a slightly decreasing in the particles' average velocity at the bend inlet with the decreasing of R/D.

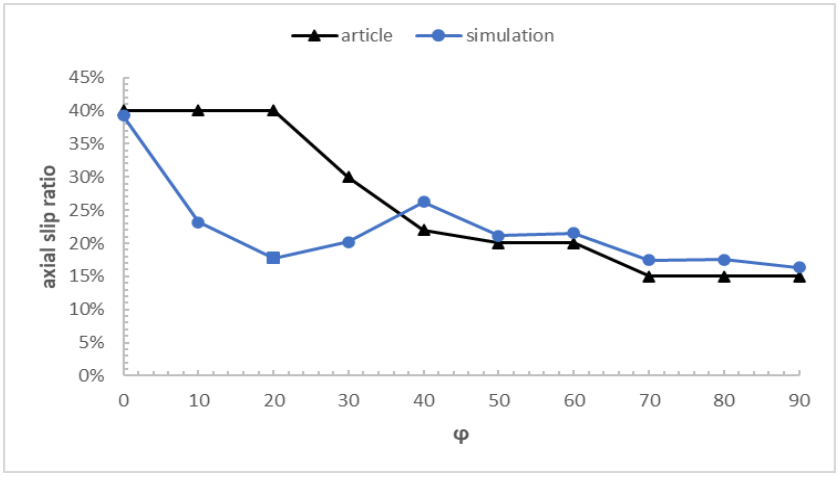

Figure 7.8: averaged particles' axial slip ratio for R/D = 6.25

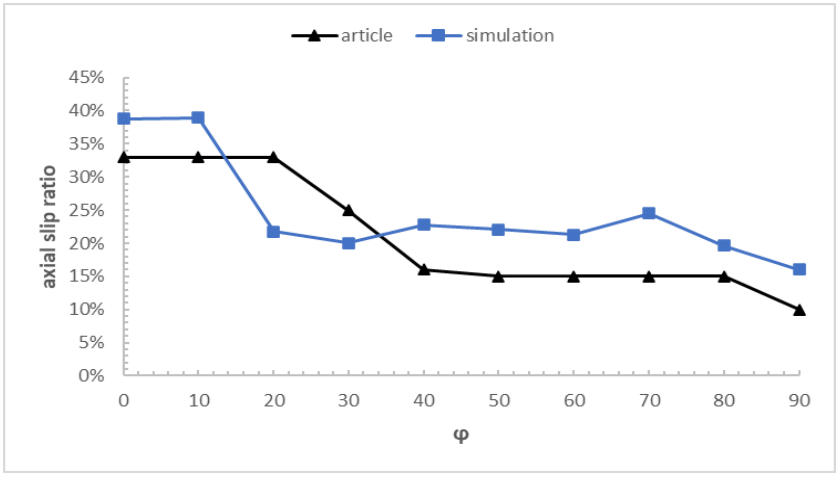

Figure 7.9: averaged particles' axial slip ratio for R/D = 5

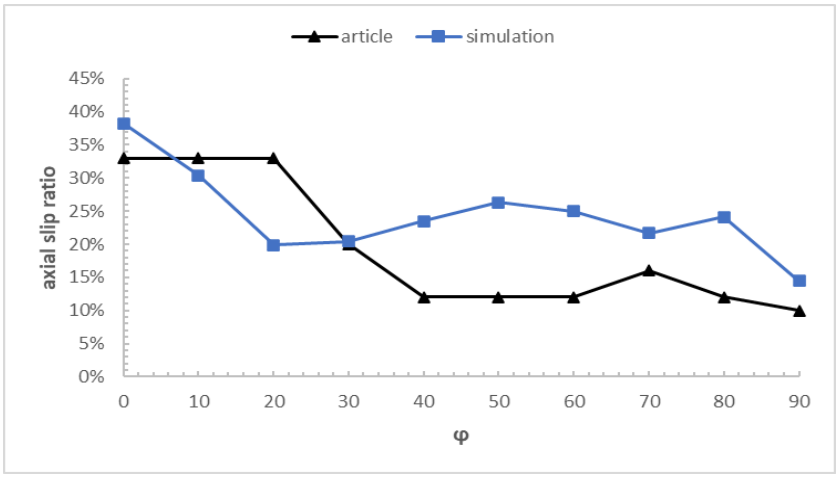

Figure 7.10: averaged particles' axial slip ratio for R/D = 3.75

In Fig. 7.11, 7.12 and 7.13 the averaged particles' axial slip ratio for all the configurations is showed, the DPM two-way-coupling is the only framework, from the ones tested, that is able to correctly evaluate the initial radial component of the particles' velocity, due to centrifugal

acceleration, which pushes the particles against the inner wall of the pipeline. Then the model predicts a reacceleration of the particles in the opposite direction before that it actually happens, as it can be seen from the experimental results, but after the region between $10 \leq \varphi \leq 30°$, the simulated values are again in good agreement with the experimental ones.

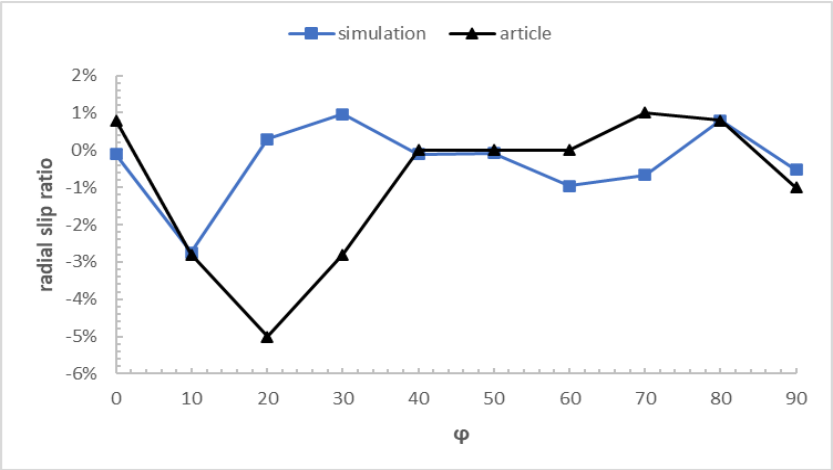

Figure 7.11: averaged particles' radial slip ratio for R/D = 6.25

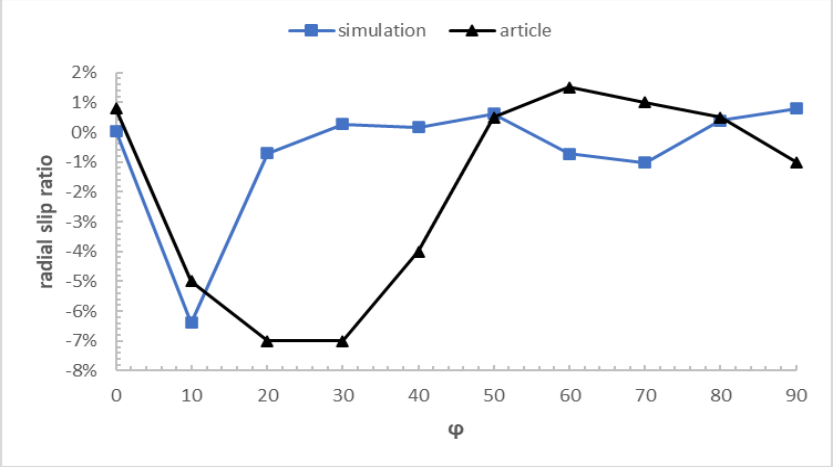

Figure 7.12: averaged particles' radial slip ratio for R/D = 5

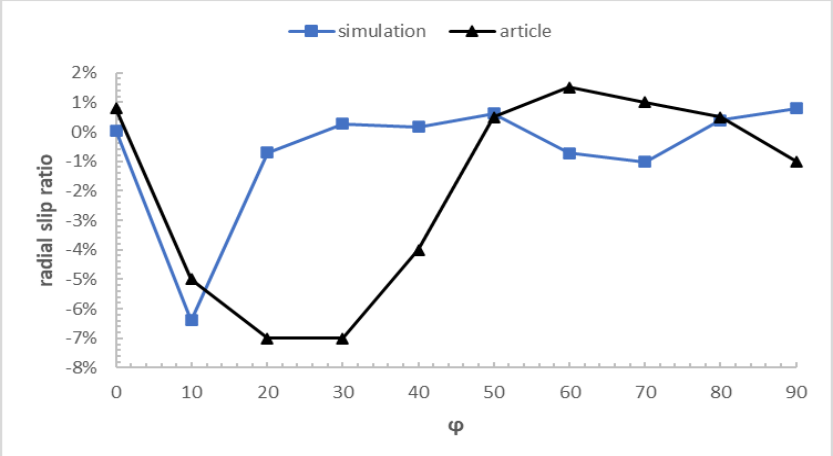

Figure 7.13: averaged particles' radial slip ratio for R/D = 3.75

In Fig. 7.14 the simulated pressure drops at the first bend are compared with the correlation reported in Section 3.5. The model is not able to give good predictions on this parameter, as large errors occur.

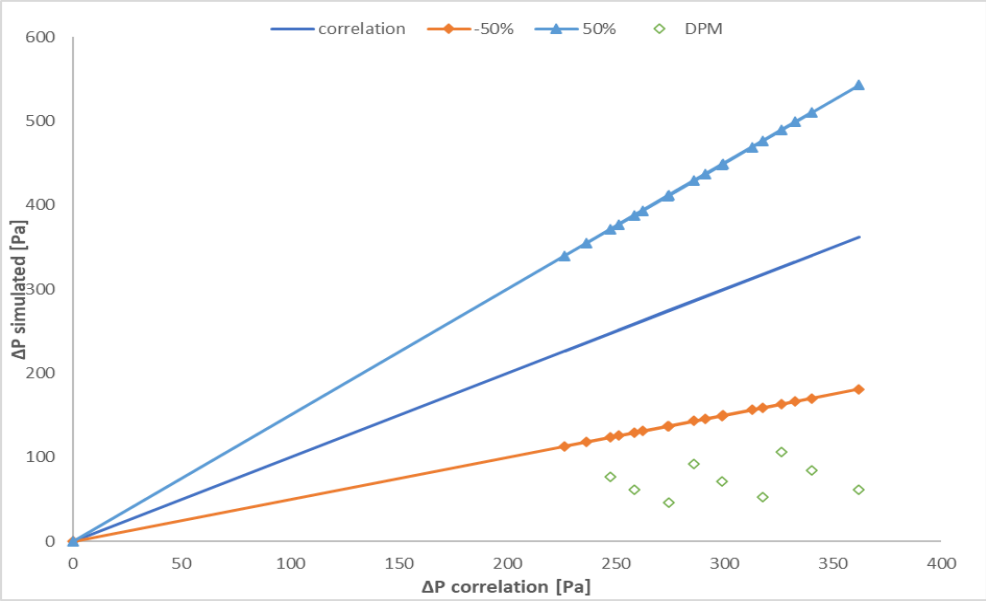

Figure 7.13: simulated vs correlation ΔP at the first bend

8. Conclusions

In this work a literature article, in which experiments on dilute phase pneumatic conveying are conducted, is investigated with three different approaches, MP-PIC, TFM and DPM, implemented respectively in the commercial software BarracudaVR and Ansys Fluent. Firstly, a tuning on the parameters on each framework is done on a specific experimental configuration, taking as reference parameter one of the macroscopical variables obtained by the article: the total line pressure. In this analysis it emerges that each model is extremely sensitive to the parameters that described the particle-wall interactions, while the particle-particle parameters have negligible impact.

Once the model is tuned the macroscopical variables of interest are obtained for each configuration, comparing the simulated values with the experimental ones. In general, the predictions of the simulations are in fair agreement with the experimental results, especially regarding the total line pressure drops.

The MP-PIC method fails to predict well particles' velocity, especially in proximity of the first bend, one explanation involves the poor mesh quality obtained in BarracudaVR in comparison to that of Ansys Fluent. The DPM gives fair predictions on particles' velocity, but fails with the bend pressure drops, which are underestimate, in contrast to MP-PIC, which in this case gives the best predictions out of the three models evaluated. The TFM is the most dependable model as no large errors on its predictions are found, this is probably due to the low solid concentration in the system.

For further analysis it could be interesting test the MP-PIC method on Ansys Fluent, where it is named DDPM, to find if the problems of this approach are only related to mesh quality issues. Moreover, it could be interesting test these models, keeping the parameters at the values determined in this work, with other experimental works that involves dilute phase pneumatic conveying to make further comparisons.

Bibliography

[1] Li K., Kuang S. B., Pan R.H., Yu A. B. 2014, Numerical study of horizontal pneumatic conveying: effect of material properties *Powder Technology*, Vol. 251 p. 15-24

[2] Massaro Sousa L., Amblard B., Tebianian S., 2022 CFD simulation for characterization and scale-up of pulsed biomass transport *Chemical Engineering Science* Vol. 255 p.12

[3] Konrad, K., 1986 Dense-Phase Pneumatic Conveying: A Review *Powder Technology*, 49, p. 1-35

[4] Rhodes, M.J., 2008 *Introduction to Particle Technology*, John Wiley & Sons Ltd., Chichester Ch second edition

[5] Klinzing, G.E., Rizk, F., Marcus, R., Leung, L.S., 2010 *Pneumatic conveying of solids,* Springer third edition

[6] Fei, Y., Tu, P., Li, X., Chen, Y., Zheng, Y., Zhu, Rui, 2021, Dynamic analysis of particles in vertical curved 90° bends of a horizontal-vertical pneumatic conveying system based on POD and wavelet transform. *Advanced powder technology: the international journal of the Society of Powder Technology*, Japan, 2021, Vol.32 (5), p.1399-1409

[7] Mason, D.J., Levy, A., Marjanovic P., 1998, The influence of bends on the performance of pneumatic conveying system. *Advanced powder technology: the international journal of the Society of Powder Technology* Vol.9, No.3, p. 197-206

[8] Hirokata, K., Shozaburo, S., 1969, Pneumatic Conveying of solids through straight pipes, *Journal of Chemical Engineering of Japan,* Vol.2, p. 211-217

[9] Br, H.T., Grace, J.R., Types of choking in vertical pneumatic systems, 1993 *Int. J. Multiphase flow* Vol.19, No.6 p. 1077-1092

[10] Rabinovich E., Kalman H., Phenomenological study of saltating motion of individual particles in horizontal particle-gas systems

[11] Boothroyd, R.G., Flowing Gas–Solids Suspensions, 1971. Chapman & Hall, London

[12] Snider D., M., 2000 An incompressible three-dimensional multiphase particle-in-cell model for dense particles flow, . *Journal of Computational Physics*, Vol.170 p. 523-549.

[13] Travis J., Harlow, F., Amsden, A., 1976 Numerical calculation of two-phase flows, *Nucl. Sci. Engr.* Vol. 61, p.1-10

[14] Harris S.E., Crighton D. G., 1994 Solutions, solitary waves and voidage disturbances in gas-fludized beds, *J. Fluid Mech.* Vol.266, 243

[15] J. Smagorinski. General circulation experiments with the primitive equations. Monthly Weather Review, 91(3):99–164, 1963

[16] Auzerais, F. M., Jackson R., Russel W. B., The resolution of shocks and the effects of compressible sediments in transient settling, 1988 *J. Fluid Mech.* Vol.195, 437

[17] BarracudaVR User Manual 22.1

[18] Wen C.Y., Yu Y.H., 1966 Mechanics of fluidization. *Chemical Engineering Progress Symposium*, p 100–111

[19] Chhabra R.P., Agarwal L., and Sinha N. K., 1999 Drag on non-spherical particles: an evaluation of available methods. *Powder Technology*, 101(3) p. 288 – 295

[20] Haider A., and Levenspiel O., 1989 Drag coefficient and terminal velocity of spherical and non-spherical particles. *Powder Technology*, 58(1) p.63 – 70

[21] Andersson B., Andersson R., Computational Fluid Dynamics for Engineers 2011 *Cambridge University Press*

[22] Dalla Valle J. M., 1948 *Micromeritics*. Pitman, London. 1948.

[23] Syamlal M., O'Brien. T. J. 1989."Computer Simulation of Bubbles in a Fluidized Bed". *AIChE Symp.* Series.85. p.22–31

[24] Garside J., Al-Dibouni M.R., 1977 Velocity-Voidage Relationships for Fluidization and Sedimentation. *I & EC Process Des. Dev.*. 16. p.206–214.

[25] Dalla Valle J. M., 1948 *Micromeritics*. Pitman, London. 1948

[26] Lun, CKK, et al. 1984, Kinetic theories for granular flow: inelastic particles in Couette flow and slightly inelastic particles in a general flowfield. *J. Fluid Mech.* 140, p. 223–256

[27] Ding J., and D. Gidaspow. 1990, A Bubbling Fluidization Model Using Kinetic Theory of Granular Flow". *AIChEJ.* Vol 36(4) p. 523–538.

[28] Gidaspow D., Bezburuah R., Ding J., 1992, Hydrodynamics of Circulating Fluidized Beds, Kinetic Theory Approach. In Fluidization VII, *Proceedings of the 7th Engineering Foundation Conference on Fluidization*. p. 75–82.

[29] Syamlal M., Rogers W., O'Brien T., 1193 J..MFIX Documentation: Theory Guide,Vol.1

[30] Ogawa S., Umemura A., N. Oshima N., 1980. On the Equation of Fully Fluidized Granular Materials. *J.Appl. Math. Phys.* Vol. 31. p.480

[31] Johnson P. C., and R. Jackson. 1987. Frictional–collisional constitutive relations for granular materials, with application to plane shearing. *Journal of Fluid Mechanics* 176:67–93.

[32] Hinze O.J., Turbulence. 1975, *McGraw-Hill Publishing Co*., New York.

[33] Elghobashi S. On predicting particle-laden turbulent flows. 1994 *Appl. Sci. Res.* 52, p. 309–329 (1994)

[34] Reynolds O., 1895, On the Dynamical Theory of Incompressible Viscous Fluids and the Determination of the Criterion. In *Philosophical Transactions of the Royal Society of London. A* pp. 123–164.

[35] ANSYS Fluent Multiphase Flow Modelling guide 2021

[36] Rui Z., Chunsheng L., Xin L., Fei Y., 2019, Experimental Quantification of Local Pressure Loss at a 90°Bend in Low-Pressure Dilute-Phase Pneumatic Conveying of Coarse Particles *International Journal of Chemical Engineering*, Vol. 2019, p. 9

Acknowledgements

Ci tengo a ringraziare la mia famiglia che mi ha sempre sostenuto in questi anni univeristari nonostante le difficoltà iniziali. Ringrazio anche i miei amici che mi hanno sempre sostenuto in questi anni, e il gruppo del Poli. Un ringraziamento ulteriori all'azienda IFP Energies Nouvelles per aver ospitato il mio stage e in modo particolare ai tutor che mi hanno seguito durante lo stage.